Very-long-period seismicity over the 2008-2018 eruption of Kilauea Volcano

Joshua A Crozier[1] and Leif Karlstrom[1]

[1]University of Oregon

November 30, 2022

Abstract

Very-Long-Period (VLP) volcano seismicity often represents subsurface magma resonance, and thus provides insight into magma system geometry and magma properties. We develop a signal processing workflow using wavelet transforms to detect and assess period, decay rate, and ground displacement patterns of a wide variety of VLP signals. We then generate and analyze a catalog of VLP seismicity over the 2008-2018 open vent eruptive episode at Kilauea Volcano, Hawaii USA. This eruption involved a persistent lava-lake, multiple intrusions and rift zone eruptions, and a climactic caldera collapse, with VLP seismicity throughout. We characterize trends in two dominant magma resonances: the fundamental mode of the shallow magma system is a vertical oscillation of the magma column in the conduit/lava-lake, and higher frequency modes largely consist of lateral lava-lake sloshing. VLP seismicity was mainly triggered by lava-lake surface perturbations, and less commonly from depth. Variation in event period and decay rate occurred on timescales from hours-years. On timescales of months or less these changes were often correlated with other datasets, such as ground tilt, SO2 emissions, and lava-lake elevation. Variation in resonant properties also occurs over days-months preceding and/or following observed intrusions and eruptions. Both gradual and abrupt changes in ground displacement patterns indicate evolution of shallow magma system geometry, which contributes to the variation in resonant modes. Much of the variation on timescales of months or less likely reflects changing magma density and viscosity, and thus could inform a variable shallow magmatic outgassing and convective regime over the ten year eruptive episode.

Very-long-period seismicity over the 2008-2018 eruption of Kīlauea Volcano

Josh Crozier[1], **Leif Karlstrom**[1]

[1]Department of Earth Sciences, University of Oregon, Eugene, Oregon, USA.

Key Points:

- Cataloging very-long-period volcano seismicity with wavelet transforms
- 2008-2018 Kīlauea Volcano magma resonance
- Comparing Kīlauea Volcano very-long-period seismicity with ground tilt, GPS, lava-lake, and SO_2 data

Corresponding author: Josh Crozier, jcrozier@uoregon.edu

Abstract

Very-Long-Period (VLP) volcano seismicity often represents subsurface magma resonance, and thus provides insight into magma system geometry and magma properties. We develop a signal processing workflow using wavelet transforms to detect and assess period, decay rate, and ground displacement patterns of a wide variety of VLP signals. We then generate and analyze a catalog of VLP seismicity over the 2008-2018 open vent eruptive episode at Kīlauea Volcano, Hawaii USA. This eruption involved a persistent lava-lake, multiple intrusions and rift zone eruptions, and a climactic caldera collapse, with VLP seismicity throughout. We characterize trends in two dominant magma resonances: the fundamental mode of the shallow magma system is a vertical oscillation of the magma column in the conduit/lava-lake, and higher frequency modes largely consist of lateral lava-lake sloshing. VLP seismicity was mainly triggered by lava-lake surface perturbations, and less commonly from depth. Variation in event period and decay rate occurred on timescales from hours-years. On timescales of months or less these changes were often correlated with other datasets, such as ground tilt, SO_2 emissions, and lava-lake elevation. Variation in resonant properties also occurs over days-months preceding and/or following observed intrusions and eruptions. Both gradual and abrupt changes in ground displacement patterns indicate evolution of shallow magma system geometry, which contributes to the variation in resonant modes. Much of the variation on timescales of months or less likely reflects changing magma density and viscosity, and thus could inform a variable shallow magmatic outgassing and convective regime over the ten year eruptive episode.

1 Introduction

Volcano seismicity provides vital information for studying processes inside volcanoes and for monitoring changes in volcanic activity that inform hazards [*Chouet*, 1996; *Ripepe et al.*, 2015]. Amongst the rich variety of seismic signals that are commonly observed at volcanoes, so-called very-long-period (VLP) seismic events are of particular interest for magmatism as they likely represent fluid oscillations in magmatic transport structures [*B.Chouet*, 2013; *McNutt and Roman*, 2015]. VLP seismicity is typically defined as having a disproportionate amount of energy at periods greater than ~2 s, often focused into one or more discrete spectral peaks. This type of seismicity can provide otherwise unobtainable in situ insight into magma properties and magma plumbing system geometry [*Chouet et al.*, 2011, 2013; *Karlstrom et al.*, 2016; *Liang et al.*, 2019a], and can be sensitive to different properties of the system than the longer timescale deformation observed with geodesy. Here we develop a signal processing workflow for cataloging VLP seismicity, and then apply this workflow to generate and analyze a catalog of VLP seismicity at Kīlauea Volcano.

1.1 Cataloging VLP seismicity

Several studies have created catalogs of long or very-long period seismicity at volcanic settings [*Battaglia*, 2003; *Aster et al.*, 2008; *Chouet et al.*, 2010; *Dawson et al.*, 2014; *Knox et al.*, 2018; *Wech et al.*, 2020], with a variety of approaches demonstrating that detecting these signals robustly requires different approaches than detecting standard tectonic earthquakes. Time-domain moving short-term-average/long-term-average (STA/LTA) type detectors will miss many signals that do not stand above the background noise level [*Schaff*, 2008]. Cross-correlation based template matching techniques can be much more sensitive [*Schaff*, 2008] and have been used to detect some types of long-period seismicity [*Aster et al.*, 2008; *Wech et al.*, 2020]. However, template matching is better suited to detecting repeating events than signals that exhibit a continuum of variation (i.e., in resonant periods, decay rates, and trigger mechanisms), and is computationally slow [*Yoon et al.*, 2015]. Approaches using feature-extraction to create and cluster waveform 'fingerprints' are computationally faster, but still best suited to detecting repeating events [*Yoon et al.*, 2015].

Supervised machine learning approaches can also be effective for detecting earthquakes [*Perol et al.*, 2018; *Jennings et al.*, 2019; *Bergen and Beroza*, 2019] and have been used to detect very-long-period seismicity [*Chouet et al.*, 2010]. However, supervised learning methods can require lots of pre-selected training examples, may not detect types of signals they were not trained on robustly, will generally need at least partial re-design and/or re-training to be applied to new networks/volcanoes, and their 'black box' nature can make predicting when or why they fail difficult [*Bell*, 2014; *Goodfellow et al.*, 2016]. Unsupervised learning methods have been used to cluster seismic data [*Kohler et al.*, 2010; *Mousavi et al.*, 2019], but have not yet been demonstrated to generate accurate/comprehensive event catalogs. They will also generally require reanalysis/reinterpretation of the output clusters when new data is added [*Bell*, 2014], and may thus be more promising as a tool to help interpret variability in already cataloged events.

Accurately categorizing VLP signals is also important, since the resonant periods, decay rates (quantified by quality factor Q, a ratio of energy stored to energy lost per cycle), and source motions (from ground displacement patterns) can encode the underlying resonant mechanism [*Liang et al.*, 2019a,b]. Q is often difficult to calculate robustly, and several methods have previously been used. The simplest is to calculate the full width at half the maximum amplitude (FWHM) of peaks in the power spectrum, though this is often not effective in the presence of noise, complicated signal shapes, or multiple signals with similar frequency components [*Kumazawa et al.*, 1990; *Zadler et al.*, 2004]. For this reason autoregressive (AR) methods that fit decaying sinusoids to the coda of signals were developed [*Kumazawa et al.*, 1990; *Nakano et al.*, 1998; *Lesage et al.*, 2002; *Dawson et al.*, 2014]. When the coda of a signal can be appropriately isolated these methods work well for classifying dominant resonant modes. However, they often do not accurately detect or estimate Q of secondary resonant modes or modes with coda interrupted by other signals (Fig. S.7). Bandpass filtering can help isolate secondary signals, but often a narrow passband would be required which will artificially increase Q [*Kumazawa et al.*, 1990].

We use continuous wavelet transforms (CWTs) to detect and classify T, Q, and ground displacement patterns of VLP seismic signals. CWTs are a method for determining the frequency content of signals over time [*Alsberg et al.*, 1997; *Selesnick et al.*, 2005] that have been previously used to analyze volcano seismicity [*Lesage*, 2009; *Lapins et al.*, 2020]. Our methods are able to robustly determine T and Q in the presence of high noise, multiple resonant frequencies, and overlapping signals. Although not the focus here, these methods are readily extendable to characterizing VLP tremor [*Chouet*, 1996; *Dawson et al.*, 2014] and gliding-frequency signals. Our approach does not depend upon training data or templates, and thus can be applied to any seismic network or volcano with minimal configuration.

1.2 2008-2018 eruption of Kīlauea Volcano

Kīlauea Volcano is an excellent study location due to the dense broadband seismic network operated by the Hawaii Volcano Observatory, which has recorded thousands of VLP events over the past two decades [*Dawson et al.*, 2014; *Liang et al.*, 2019b]. There is also a wealth of other available data including direct observations of the Halemaʻumaʻu summit lava-lake during these events [*Orr et al.*, 2013; *Dawson et al.*, 2014]. We examine the 2008-2018 eruptive episode, the most recent period of continuous summit activity following decades of quiescence or sporadic events largely focused along the East-Rift-Zone (ERZ) [*Wright and Klein*, 2014]. Over this timespan a summit lava-lake persisted at the surface, then drained as part of a caldera collapse eruption sequence in May-August 2018 [*Neal et al.*, 2019; *Patrick et al.*, 2019a,b]. VLP seismicity at Kīlauea has previously been cataloged up to 2013 using a hidden Markov model to detect events and the Sompi AR method to determine T and Q of these events [*Dawson et al.*, 2014]; this existing catalog provides an important benchmark for our methods.

We find prevalent VLP seismicity over the whole 2008-2018 timespan, with VLP T, Q, and ground displacement patterns varying over timescales from hours to years. We compare our VLP catalog to other datasets such as lava-lake elevation, tilt and GPS (which measure summit reservoir inflation), SO_2 emissions, and observations of rift zone eruptions and inferred intrusions. This yields insights into how known changes in the magma system are reflected in seismicity, and indicates additional changes on a variety of timescales.

2 Methods

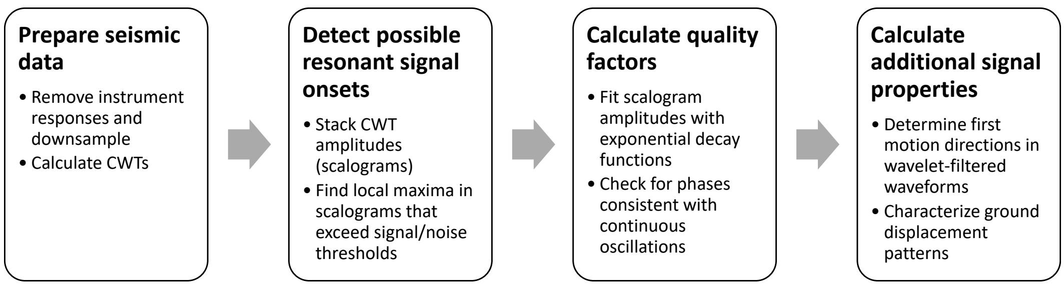

Figure 1. Signal processing workflow for VLP detection and characterization.

2.1 Seismic data

Near-field broadband seismometers are best suited for picking up the often low amplitude long-period signals of interest to VLP studies. We use waveforms from 3-component broadband seismometers in the Hawaii Volcano Observatory (HVO) network [*USGS*, 1956] that are within ~3 km of the vent. We use available data from the following stations: NPB, NPT, SRM, OBL, WRM, SDH, UWE, UWB, SBL, KKO, and RIMD (Fig. 2, 10). Some other stations in the area were not used due to low signal/noise ratios. Data from 2008-2011 was obtained from the USGS, subsequent data is publicly available from IRIS (Incorporated Research Institutions for Seismology). We download and process data in 6 hr time windows. There are gaps in data availability for many of these stations; data gaps of less than 2 s duration are filled by linear interpolation and waveforms with larger gaps are discarded.

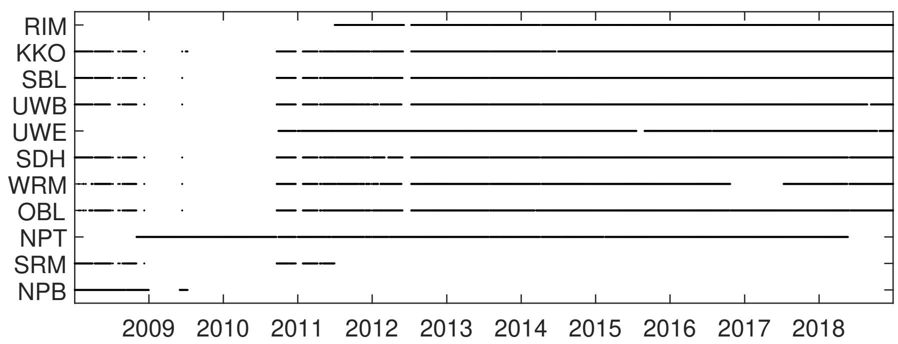

Figure 2. Timeline of data availability at the HVO broadband seismic stations used in this study.

In order to combine data from different instruments, we must deconvolve the instrument responses. A standard 'water level' is first applied to these instrument responses so that the maximum amplification is 10 times the base amplification. This prevents overmagnification of noise at periods longer than the instrument sensitivity ranges. We note that this process is not causal and can introduce artificial tapers around discontinuities (i.e., step functions); an effect included in the synthetic seismograms we use to test our methods (Appendix A:). To facilitate stacking and faster processing, all waveforms are then smoothed with a 'lowess' moving linear regression and resampled at 6 Hz. Lowess smoothing conformed to sharp discontinuities without introducing artificial oscillations better than other smoothing we tested such as FIR and IIR filters or moving quadratic regressions.

2.2 Continuous wavelet transforms

Time-frequency representations of data are well suited to identifying resonant signals [*Köcher et al.*, 2014]. A spectrogram is the simplest such representation, obtained from the amplitudes of a short-time Fourier transform (STFT) which consists of discrete Fourier transforms (DFTs) calculated over sequential time windows. However, there are disadvantages to STFTs that make continuous wavelet transforms (CWTs) better for our purposes. Other methods for time-frequency analysis such as the Wigner-Ville distribution and Hilbert-Huang transform have been applied to seismic data [*Lesage*, 2009], but we found them less useful than CWTs for our purposes.

CWTs involve specifying a base wavelet that can be stretched or 'scaled' to different frequencies and cross-correlated with data to determine frequency content as a function of time [*Alsberg et al.*, 1997; *Selesnick et al.*, 2005]. Plots of CWT amplitudes are termed scalograms. For a given wavelet, CWTs provide increasing temporal resolution with increasing frequency. This is one advantage over STFTs, which for a given window length provide the same temporal resolution for all frequencies, introducing an unnecessary trade-off between temporal resolution of high frequencies and spectral resolution of low frequencies.

Useful wavelets for time-frequency analysis are often sinusoids scaled by some function with symmetric, compact support so as to decay in both directions from a central point (Fig. 3). Wavelets with more gradual decay (i.e., more oscillations) will provide better frequency resolution but worse temporal resolution (Fig. 3), analogous to increasing window length in a STFT. An arbitrarily number of 'stretches' of a wavelet can be used to sample at any desired frequencies, though there is a limit to the effective frequency resolution possible with a given wavelet width. The gradual onset of wavelets introduce less artificial temporal 'jaggedness' than a standard STFT, since a STFT uses sinusoids that terminate abruptly at the edges of each time window. This smoothness allows for more accurate determination of signal decay rates.

The convolution between a wavelet and an impulsive signal (such as a single peak) will have a duration and decay rate similar to the wavelet itself (Fig. S.6), analogous to how STFTs will cause impulsive signals to appear spread in time over the window length used. This means that the wavelet duration and decay rate will determine the minimum signal duration and Q that can be distinguished from an impulsive signal, with narrower wavelets being able to resolve shorter and lower Q oscillations.

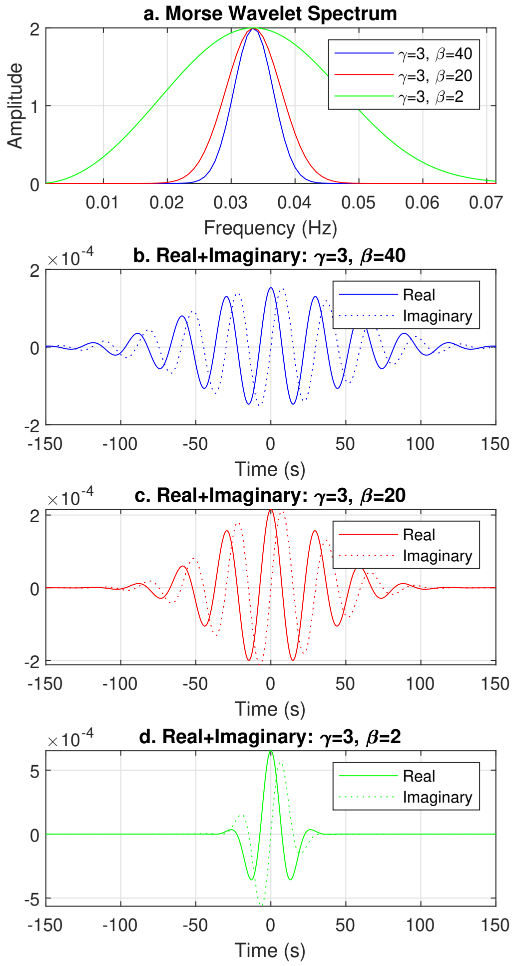

Figure 3. Morse wavelets used in this study (in this case scaled to a period of 30 s). The $\beta = 40$ (plot b) and $\beta = 20$ (plot c) wavelets are both used to make combined scalograms from which potential VLP signals are detected. The $\beta = 20$ wavelet is also used for calculating Q of signals. The $\beta = 2$ (plot d) wavelet is used for detecting first motions of signals.

We use Morse wavelets which are given in the spectral domain (for angular frequency ω) by:

$$\Psi_{\beta,y}(\omega) = U(\omega) a_{\beta,y} \omega^{\beta} e^{-\omega^{\gamma}} \tag{1}$$

where $U(w)$ is the Heaviside step function, β is a parameter that governs wavelet duration (number of oscillations), γ is a parameter that governs wavelet symmetry, and $a_{\beta,y}$ is a normalizing constant [*Lilly and Olhede*, 2009]. We set $\gamma = 3$ which yields wavelets that are symmetric in the frequency domain [*Lilly and Olhede*, 2009].

2.3 Detecting potential resonant signal onsets

To mitigate the inherent trade-off between spectral and temporal resolution we make combined scalograms using wavelets with two different values of β, 40 and 20 (Fig. 3). The $\beta = 40$ wavelet provides higher frequency resolution which helps more accurately determine resonant signal period. The $\beta = 20$ wavelet provides better time resolution while still providing enough frequency resolution to isolate typical VLP signals (Fig. S.4). Better temporal resolution helps determine onset times, reveal gaps in a signal which could indicate that it is not continuous resonance (Fig. S.5), and distinguish low Q resonance from impulsive signals (Fig. S.6).

We then stack the scalograms from all available stations to increase the signal/noise ratio. We exclude periods less than 10 s in this study because of the strong oceanic microseism at these periods [*Berger et al.*, 2004; *Dawson et al.*, 2014]. Given the proximity of our stations, delays from seismic wave propagation will be minimal relative to the periods of interest. For reference, at wave-speeds of 1800 m/s (a reasonable estimate for shallow s-wave speed at Kīlauea [*Dawson et al.*, 1999; *Lin et al.*, 2014]) a wave with a 10 s period will have a wavelength of 18 km, roughly four times the distance across our array (~5 km). There is also no concern about destructive interference from stacking scalograms since they contain no phase information.

To detect potential resonant signal onsets in a stacked scalogram, we first calculate moving long-term averages (LTA) and moving standard deviations of each frequency component with 200 s windows (Fig. 4). We then introduce a frequency-dependent delay of four cycles to the LTA and standard deviation values to account for non-causality introduced by the wavelets. Next we identify all local maxima in the stacked scalogram separated by at least 200 s in each frequency band (Fig. 4). Finally, we keep only the local maxima with amplitudes that are above some chosen multiple of the LTA (which we refer to as the STA/LTA threshold), and that are also more than some threshold number of standard deviations above the LTA. We select a threshold of 3 for both; chosen to minimize noise (or false positives) while still keeping most desired signals in both synthetic tests and real data (Fig. S.3, S.10, S.11). Where local maxima occur at adjacent periods or with periods separated by less than a factor of 1.07 (the minimum separation in periods that can be robustly resolved with the wavelets we use), we keep the maxima corresponding to the highest energy integrated over the following two cycles, which is more robust than just keeping the highest maxima (Fig. 4).

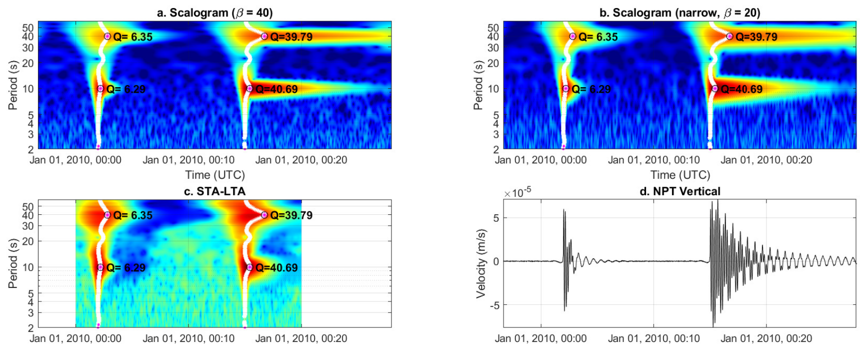

Figure 4. Example scalograms and detected resonant signals from synthetic scalograms (Appendix A:). This synthetic seismogram (plot d) consists of four VLP signals with [start time, T, Q] = [00:05, 40, 6], [00:05, 10, 6], [00:15, 40, 40], [00:15, 40, 40], plus white noise from a standard normal distribution scaled by 0.1% of the signal amplitude. We note that the slight precursory oscillations that arise from removing the instrument response. White dots in scalograms (plots a, b, and c) indicate temporal local maxima that meet the minimum STA/LTA criteria, and magenta dots indicate points that are spectral local maxima (integrated over two cycles). Black circles and text indicate the final selected resonant signal onsets and corresponding calculated Q. Here T and Q of all resonant signals are recovered accurately.

2.4 Calculating the quality factor (Q) of resonant signals

We calculate Q by fitting decaying exponentials to stacked scalogram amplitudes following each detected potential resonant signal onset (Fig. 5). We use only the narrower $\beta = 20$ CWTs that have better temporal resolution (Fig. 3); the minimum Q that this wavelet can robustly resolve is around 6. We extract scalogram amplitudes at the target frequency over one to eight cycles after the identified signal onset. The one cycle delay avoids the region near the onset of an impulsively initiated signal where amplitudes will be inherently underestimated (since part of the wavelet will not be overlapping the signal), and also helps avoid artifacts that might be present from a resonance trigger mechanism.

A standard least-squares exponential regression could underestimate decay rate in the presence of noise or where another signal starts within the fitting window (Fig. S.8). We instead solve for the exponential curve with initial amplitude fixed to the initial scalogram amplitude $A(t_1)$ and with the slowest decay rate g that remains under all of the scalogram amplitudes in the timespan being fit (t_1 to t_2) (Fig. 5, S.8):

$$g = \min_{t=t_1}^{t_2} \left(\frac{\ln\left(A(t)\right) - \ln\left(A(t_1)\right)}{t - t_1} \right) \tag{2}$$

which then yields quality factor: $Q = -\pi/(Tg)$. This fitting method is also less sensitive to the choice of fitting timespan than a least-squares regression would be. Extending the timespan will have no effect unless the added amplitudes fall beneath the current fit.

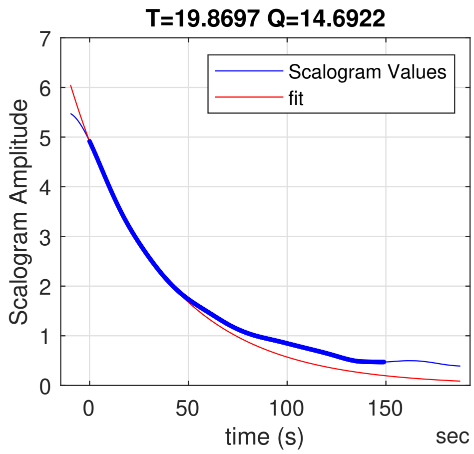

Figure 5. Example estimation of Q by scalogram exponential fit from a synthetic seismogram. This seismogram consists of a VLP signal with $[T, Q]$ = [20 s, 15], plus white noise from a standard normal distribution scaled by 0.1% of the signal amplitude. The bold part of the blue line shows the part of the scalogram data that is being fit.

Since this method does not account for phase, non-continuous oscillations that are close in time might not be distinguished from true resonance. To mitigate this we also extract the phases of the $\beta = 20$ CWTs at each channel and check for consistency over the timespan being fit. For a continuous oscillation, the phase (θ) of a wavelet stretched to the oscillation frequency f will increase steadily as it is convolved with the signal (Fig. 6, S.9):

$$\theta_{\text{expected}}(t) = 2\pi f t + \theta(0) \tag{3}$$

A signal that is not a continuous sinusoid can exhibit deviations from this expected phase (Fig. 6). To quantify how 'continuous' a signal is, we calculate the mean deviation from the expected phase over the timespan $(t_0 - t_1)$ being fit and over all N channels:

$$\text{mean phase deviation} = \frac{1}{N}\frac{1}{t_1 - t_0}\sum_{n=1}^{N}\int_{t_0}^{t_1}\left|2\pi f t + \tilde{\theta}_n - \theta_n(t)\right|dt \tag{4}$$

where $\tilde{\theta}_n$ is the constant phase offset that minimizes phase deviation at channel n. We use this this phase offset instead of the actual initial phase $\theta_n(t_0)$ in case there are source effects or strong noise present at the start of the timespan. We then keep only signals with a mean phase deviation of less than a threshold value of 0.1 radians. This threshold minimized noise or other discontinuous signals while still keeping most continuous resonant signals in tests on both synthetic and real data (Fig. 6, S.9, S.10, S.11).

We note that these methods are not designed for detecting or characterizing gliding-frequency signals. However, the methods introduced here could be readily modified to characterize gliding-frequency signals, since time-frequency analysis is the most intuitive way to examine such signals [*Köcher et al.*, 2014]. This would involve first tracing T over time from scalograms, which while straightforward in concept would need to be implemented in a manner that is robust in the presence of complicated signals and noise. The exponential fit could then be applied to these traces to calculate decay rates, and the expected phase at each time could be adjusted according to changing T to check whether the gliding-frequency signal is likely a continuous oscillation.

2.5 Comparison with previous Kīlauea VLP catalog

We compare our catalog to one produced using the automated detection (via a hidden Markov model trained on example events [*Dawson et al.*, 2010]) and classification (via the Sompi AR model *Kumazawa et al.* [1990]) methods of *Dawson et al.* [2014], extended through 2018. For both catalogs adjustment of various 'quality thresholds' is required to exclude excessive amounts of likely false picks. In our catalog we use thresholds: STA/LTA > 3, standard deviations above LTA > 3, and mean phase deviation < 0.1 radians. In the catalog extended from *Dawson et al.* [2014] the most useful parameters to threshold are event amplitude at station NPB or NPT and the standard deviation of Q from the Sompi fits. We set these thresholds to 400 counts and 0.25 so that this catalog contains a similar number of events to our catalog (~3200); but note that stricter thresholds would result in lower apparent scatter. In both catalogs changing these thresholds will greatly vary the number of events included, and less strict thresholds will include tens of thousands of additional events (Fig. S.10, S.11). For the thresholds used, the two catalogs

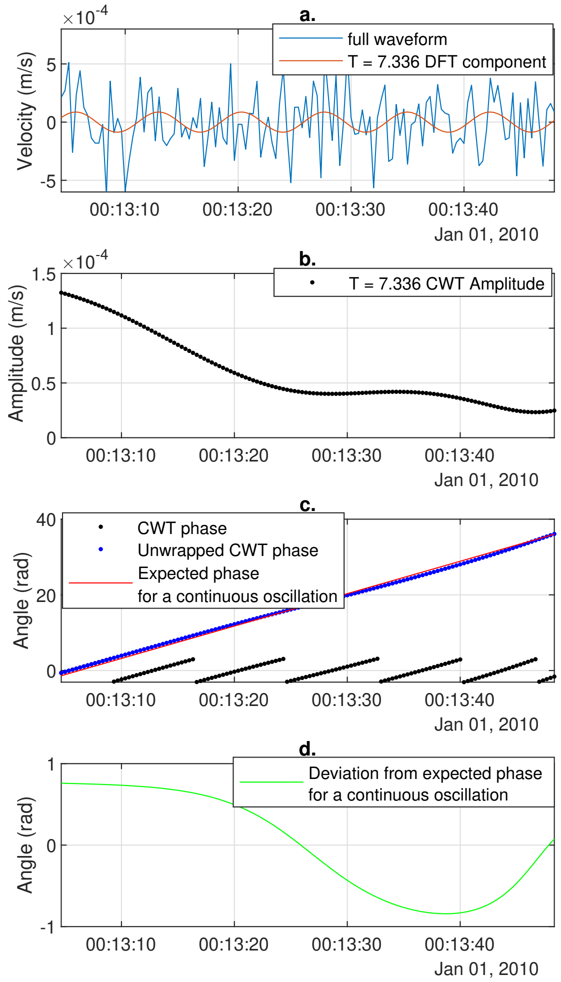

Figure 6. Example phase continuity from a spectral peak in synthetic random noise. In a scalogram (or frequency spectrum) this signal appears to contain a potential VLP event, but the high phase deviation (plot d) correctly indicates that it is not a continuous oscillation.

include around 1000 overlapping signals (Fig. 7, 8). Both catalogs also include a similar number of events that appear likely to be false detections, based on visual inspections of events in various parts of the parameter space.

Both catalogs detect a similar trend of signals with T of ~20 s in 2010, increasing to ~40 s by 2012 and remaining around 40 s until 2018. Since *Dawson et al.* [2014] use a Markov model that was trained specifically for events in this trend, it might be expected to detect some of these events with lower signal/noise ratios than our more general

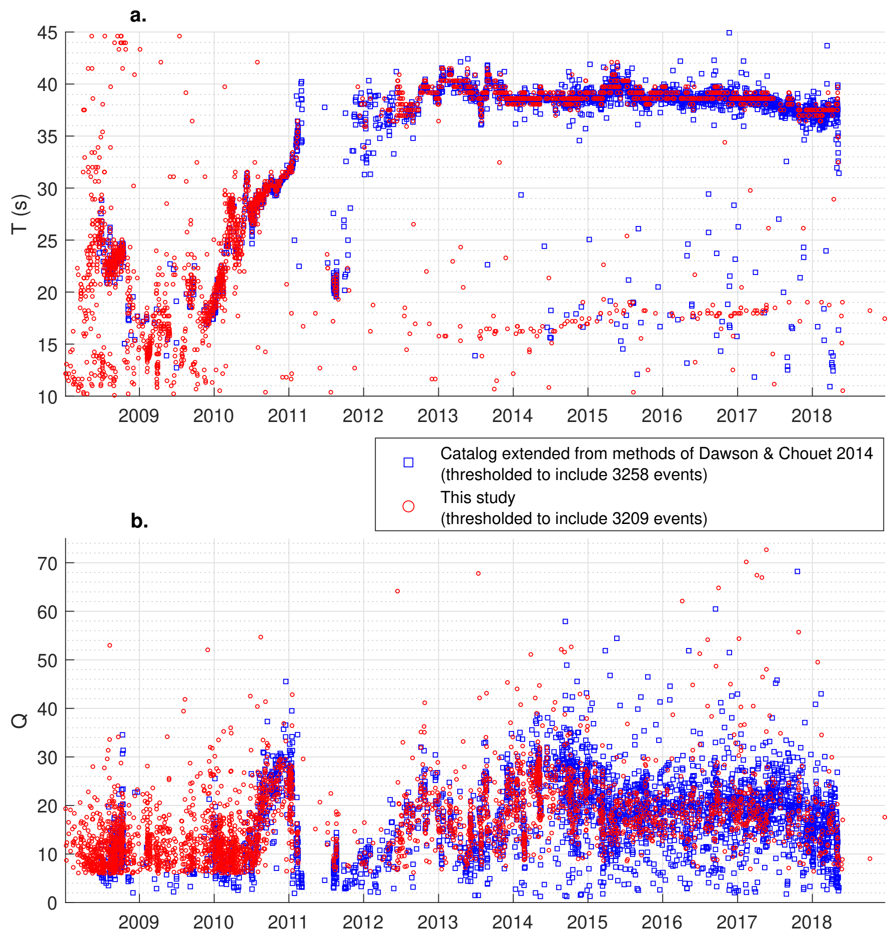

293 **Figure 7.** Comparison of detected VLP events from this study with a catalog extended from *Dawson et al.*
294 [2014]. Event detection thresholds were chosen for the catalog extended from *Dawson et al.* [2014] that pro-
295 duced a similar number of events to our catalog; orders-of-magnitude more or less events would be present in
296 either catalog depending upon the thresholds chosen (Section 4.1, Fig. S.10, S.11).

STA/LTA based approach can detect without also introducing excessive false detections. There are indeed a number of these events unique to the catalog extended from *Dawson et al.* [2014], but also many of these events unique to our catalog. This may be partly because our approach leverages data from multiple stations to increase signal/noise ratios, and partly due to limitations of the Markov model detection approach.

Our catalog also includes some additional unique clusters of signals. These include a clear cluster with T ~15 s in early 2009, and some other more isolated clusters between

2008 and 2010 (Fig. 7). Most prominently, our catalog also includes a band of signals with T ~10-20 s between 2010 and 2018 (Fig. 7). Some of these events that coincide with a 40 s event are picked up by the Sompi AR method [*Dawson et al.*, 2014], but even where they are detected the Sompi AR method often does not produce accurate estimates of Q for such secondary signals.

Our catalog appears to exhibit more scatter in T prior to 2010, but many of these values do appear to represent real signals. Both catalogs show a number of isolated signals after 2011 with T from ~10-15 and ~20-35 s. Most of these signals in our catalog appear to be from gliding-frequency VLP events; some in the catalog extended from *Dawson et al.* [2014] also are related to gliding-frequency events whereas some appear to be noise.

A final notable difference between the two catalogs is in estimates of Q. As discussed in section 2.3, our method cannot robustly detect events with $Q < 6$ given the wavelets we are using. However, low Q signals cannot be as accurately characterized anyways, since T cannot be very accurately determined for a small number of oscillations. The large scatter in T from late 2011-early 2012 in the catalog extended from *Dawson et al.* [2014] likely reflects this limitation. Estimates of Q often differ between the two methods even for matching events (Fig. 8), though neither method shows a bias for higher or lower values than the other. Where the two methods estimate appreciably different values of Q we find that there is often some complication (such as overlapping signals or strong noise) that causes the Sompi AR method to be inaccurate where our method still produces reasonable estimates of Q.

2.6 Determining first motion directions

The first motions of a signal are not well defined for signals without impulsive onsets. Even for impulsive onsets, picking first motions for a particular frequency component is difficult to do robustly because band-pass filtering a signal will distort the onset of that signal regardless of the filter used (i.e., causal or acausal, FIR or IIR) (Fig. 9). We use a ‘wavelet filter’: we compute the CWT of a signal, then reconstruct the signal using an inverse CWT but keeping only the period of interest. This still produces artificial precursory oscillations in front of signals with impulsive onsets (Fig. 9), but the size of these oscillations are predictable for a given wavelet (Fig. 3), even when the signal onset involves step

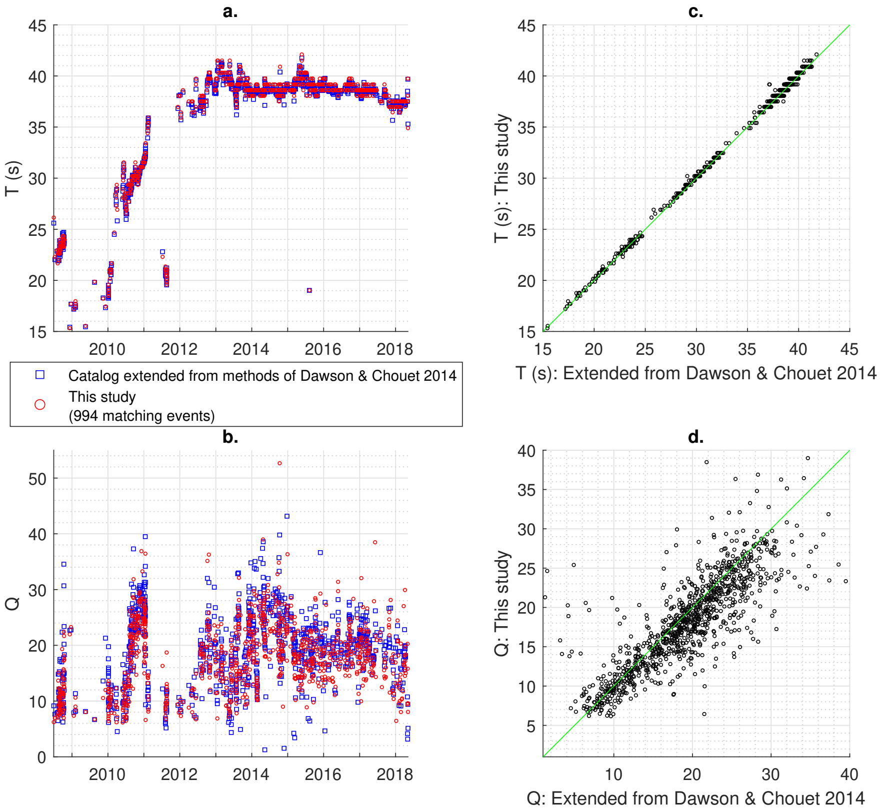

Figure 8. VLP events from this study that correspond to events in a catalog extended from *Dawson et al.* [2014]. Corresponding events have start times within 3 minutes of each other, and T ratios within 4/5-5/4 of each other. Green lines in plots c and d indicate 1:1 values.

displacements. We use a very narrow Morse wavelet ($\beta = 2$) in order to minimize precursory oscillations, though such a narrow wavelet will be more sensitive to surrounding frequencies (Fig. 3). This method will thus only work well for signals that are the dominant oscillations in their frequency band.

We then stack the amplitudes of the wavelet-filtered signals from all channels, and identify local maxima around the signal onset time that exceed thresholds for both STA/LTA and number of standard deviations above the LTA (Fig. 9). We discard local maxima that are less than half of the maximum amplitude, which will exclude precursory oscillations caused by the wavelet filter for impulsive onset signals. If one or more maxima remain we select the first of these as the first motion time, and select corresponding first motion directions at each channel from the wavelet filtered waveforms (Fig. 9). We store the

STA/LTA ratio and standard deviations above the LTA for this local maximum as indicators of pick confidence. If no suitable local maxima are found, which occurs if the signal has a gradual onset or is contaminated by other signals/noise, we label the first motions undetermined.

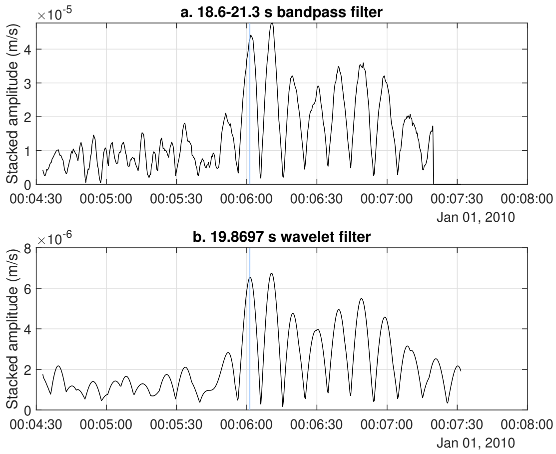

Figure 9. Example first motion pick from a synthetic seismogram for an impulsive onset oscillation with [start time, T, Q] = [00:06, 20, 20], plus a step displacement (velocity spike) at time 00:06, plus two other equal-amplitude resonant signals with [start time, T, Q] = [00:05, 80, 20] and [00:05, 5, 20], and plus white noise from a standard normal distribution scaled by 0.1% of the signal amplitude. Plot a shows stacked amplitudes from waveforms filtered with an FIR bandpass filter; this is not used for picks and is just shown for comparison. Plot b shows stacked amplitudes from waveforms filtered with the wavelet filter we use for picking first motions. The cyan line is the algorithm's correct first motion pick for the target signal.

2.7 Characterizing ground displacement patterns

Average phases and amplitudes at each channel are obtained using the Goertzel DFT algorithm [*Proakis and Monolakis*, 1990] over a time window between one and five cycles after each signal onset. Our goal in this study is not to conduct detailed source inversions for every resonant signal, but rather to quantitatively characterize changes in ground displacement patterns between VLP events. The simplest metric we use is the average vertical/horizontal velocity ratio, defined for a given frequency f as:

$$\text{vertical/horizontal} = \sum_{m=1}^{M} \frac{|\dot{u}_{Z,m}(f)|}{|\dot{u}_{E,m}(f) + \dot{u}_{N,m}(f)|} \tag{5}$$

for vertical (Z), east (E), and north (N) velocities ($\dot{u}$) at all M stations. This metric is very simple and requires no assumptions of source location or mechanics, but it is sensitive to tilt which will increase the apparent amplitude of horizontal components at increasing T.

We also quantify how radially symmetric horizontal motion vectors are by calculating the angles from the direction to an inferred source location. We set this location based on a previous geodetic (InSAR, GPS, and tilt) inversion for the shallow ground deflation source in early 2018 [*Anderson et al.*, 2019] (Fig. 10), which is similar to the shallow source location inferred by other seismic and geodetic inversions over the past decade [*Chouet et al.*, 2010, 2011; *Anderson et al.*, 2015; *Anderson and Poland*, 2016; *Liang et al.*, 2019b]. We then calculate the mean angle between observed $\dot{u}$ and predicted $\dot{w}$ velocity vectors as:

$$\text{radial misfit} = \frac{1}{M}\sum_{m=1}^{M}\int_0^{2\pi}\left|\arccos\left(\frac{\dot{u}(t)\cdot\dot{w}(t)}{|\dot{u}(t)||\dot{w}(t)|}\right)\right|dt \tag{6}$$

The final method we use to quantify ground displacement patterns is conducting source inversions for an inflating/deflating spherical reservoir using a quasi-static 'Mogi' model for a point source in an elastic half-space [*Mogi*, 1958; *Segall*, 2010]. Multiple previous seismic and geodetic studies have supported a spherical or ellipsoidal reservoir geometry [*Baker and Amelung*, 2012; *Anderson et al.*, 2015; *Anderson and Poland*, 2016; *Liang et al.*, 2019b], though some other seismic studies have instead inferred intersecting dikes [*Chouet et al.*, 2011]. Since many studies support a sphere-like reservoir, and because inversions for these VLP signals with more complex source models such as full moment tensors or dikes are often not well constrained, we focus only on the spherical reservoir model. Due to their simplicity, the Mogi source inversions are most useful as a metric of relative changes in source centroid depth between events rather than as a probe of detailed reservoir shape. In general changes in inferred Mogi centroid depth could represent changes in the vertical extents of a spherical/ellipsoidal reservoir, and/or changes in the geometry or activation of any secondary dike/sill structures that may also be contributing to the ground displacement patterns. The misfit of predicted and true displacements from Mogi inversions also provides a second metric for the radial symmetry of ground displacement patterns.

We include ground tilt (detected as horizontal acceleration by broadband seismometers) in the Green's functions [*Maeda et al.*, 2011] to predict displacements w as:

$$w(f) = \left(\mathbf{G}^{trans} + \mathbf{G}^{tilt}\frac{g}{(i2\pi f)^2}\right)P(f), \tag{7}$$

where $\mathbf{G}^{trans}$ and $\mathbf{G}^{tilt}$ are the tilt and translation Green's function matrices, g is gravitational acceleration, and P is forcing pressure. We can then solve for the P that best fits observed displacements u for a given set of Green's functions using a linear least-squares inversion.

We again fix the east and north source location based on previous geodetic inversions [*Anderson et al.*, 2019] (Fig. 10). We assume a shear modulus of 10 GPa and Poisson's ratio of 0.25. We then conduct a grid search over source depth between 500-2500 m beneath the caldera floor, choosing the depth that minimizes misfit according to:

$$\text{misfit} = \frac{\sum_{n=1}^{n} |w_n(f) - w_n(f)|}{\sum_{n=1}^{n} |u_n(f)|} \tag{8}$$

for all N channels.

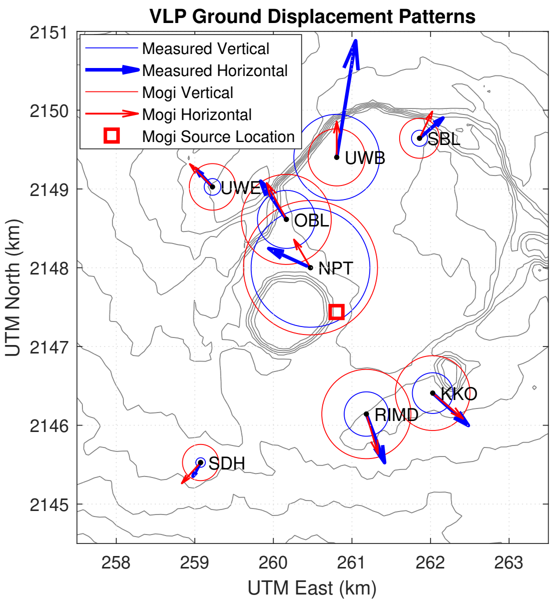

Figure 10. Ground displacements and Mogi inflating spherical reservoir source inversion for an example conduit-reservoir event on 2017-5-21 at the time of peak vertical displacement at station NPT. Displacements are from integrated seismic velocities, so horizontal components in the data and source inversion include both tilt and translation effects.

2.8 Other data

ERZ eruptions prior to 2018 have been compiled in *Patrick et al.* [2019b]: the March 2011 Kamoamoa fissure eruption [*Orr et al.*, 2015], August 2011 Puʻu ʻŌʻō vent opening, September 2011 Puʻu ʻŌʻō vent opening, June 2014 Puʻu ʻŌʻō vent opening [*Poland et al.*, 2016], and May 2016 Episode 61g Puʻu ʻŌʻō vent opening [*Chevrel et al.*, 2018]. Timing of the 2018 eruption is given in *Neal et al.* [2019]. Documented summit intrusions have been compiled in *Patrick et al.* [2019b]: October 2012, May 2014, and May 2015 [*Johanson et al.*, 2016]. Regional slow-slip events (SSEs) have been compiled in *Montgomery-brown et al.* [2015] and *Wang et al.* [2019]: February 2010, May 2012, and October 2015.

To indicate long-term ground deformation we use data from near-field (within ~2 km of the vent) GPS stations (vertical displacements from station HOVL and horizontal line-lengths between stations UWEV and CRIM [*Miklius*, 2008]) and tilt-meters (east and north tilt from station UWE [*Johanson*, 2020]). To infer ground inflation-deflation trends, we combine the GPS and tilt-meter data. We first smooth all four datasets with 30-day moving average filters. We then resample each dataset at 1-day periods and rescale each dataset to have a unit range. Lastly, we flip the sign of UWE east tilt-meter data (since eastward tilt at this station corresponds to ground deflation), and stack the four datasets. We then consider times when the stacked value is positive to represent long-term ground inflation, and negative to represent long-term ground deflation.

Lava-lake elevation data is obtained from webcam images, thermal images, and laser rangefinder data [*Patrick et al.*, 2019b] (data extended through 2018 was obtained from the USGS). We also include estimates of lava-lake surface area from *Patrick et al.* [2019b].

SO_2 is generally the most easily measurable major volcanic volatile species, and is an important indicator of magmatic processes [*Sutton and Elias*, 2014]. SO_2 data from various monitoring stations for the whole timespan does exist *Whitty et al.* [2020], but we only consider data from published studies using direct measurements of the summit plume. We use SO_2 emission data collected by a vehicle-based FLYSPEC UV spectrometer from 2007-2010 [*Elias and Sutton*, 2012]. We also use SO_2 emission data collected by an array of FLYSPEC UV spectrometers from 2014-2017 [*Elias et al.*, 2018]. Both datasets have large uncertainties (Fig. 13, 14) due to spectral fitting limitations and uncertainty in plume speed and location [*Elias and Sutton*, 2012; *Elias et al.*, 2018].

We also analyze the time-derivatives of some of these datasets. Comparing time-derivatives can sometimes better reveal short-term correlations, particularly when gradual or punctuated changes in the relation between two variables causes the direct correlation over long timespans to exhibit large scatter. Since derivatives are inherently more sensitive to high frequency noise, we calculate time-derivatives using FIR differentiator filters with 7-day corner periods.

3 Results

3.1 Types of VLP seismicity at Kīlauea from 2008-2018

We will introduce the common types of VLP signals present in the catalog to facilitate discussion in the following sections.

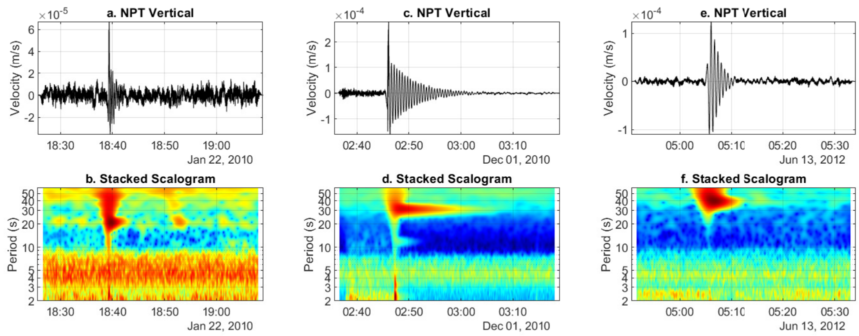

Figure 11. Example VLP signals. (Plots a and b) Normal conduit-reservoir mode event along with background VLP tremor from January 2010, when the lava-lake became persistent [*Patrick et al.*, 2019b]. The event had an impulsive broadband onset and inflationary first motions, indicative of a rockfall trigger. The background VLP tremor had the same dominant period as the impulsively triggered VLP event, but often unclear onsets and no higher frequency triggers. (Plots c and d) Normal conduit-reservoir event with secondary lava-lake-sloshing mode from December 2010, two months before the March 2011 Kamoamoa fissure eruption. This event had an impulsive broadband onset and inflationary first motions indicative of a rockfall trigger. There was also background tremor at periods less than around 3 s that was truncated by this event. (Plots e and f) Reverse VLP event from June 2012, shortly after the May 2012 SSE. This event had an impulsive onset but no high frequency trigger. There was a small initial inflationary motion but the first large oscillation was deflationary.

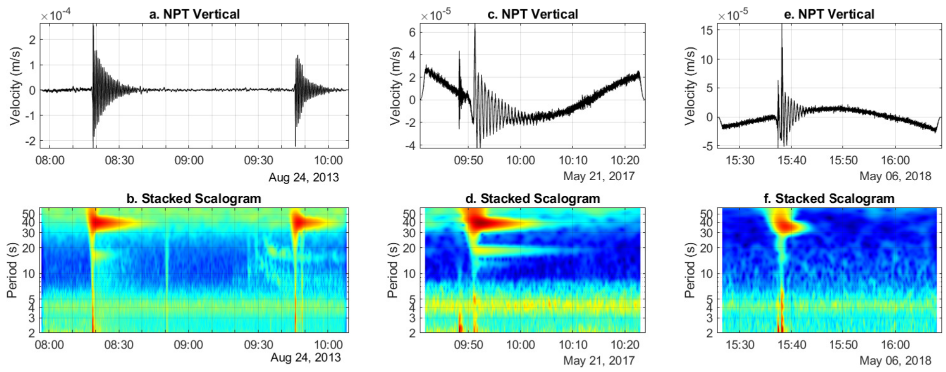

Figure 12. Example VLP signals. (Plots a and b) Normal and Reverse conduit-reservoir modes and lava-lake-sloshing mode from August 2013. The Normal conduit-reservoir mode started at around 7:50 with an impulsive inflationary broadband trigger indicative of rockfall, and with an accompanying lava-lake-sloshing mode. The Reverse conduit-reservoir event occurred 90 minutes later, with no concurrently triggered lava-lake-sloshing, and appears to be partially truncated around 5 minutes after it's onset. A gliding-frequency VLP signal started about 20 minutes before the second event, with no apparent trigger and a final period similar to the previous lava-lake-sloshing mode. (Plots c and d) Normal conduit-reservoir event with two lava-lake-sloshing modes from May 2017. A higher frequency impulsive signal occurred about 2 minutes before these resonant modes that may have been related to their triggering. (Plots e and f) Normal VLP event from May 2018, 4 days after the lava-lake began draining. This event exhibited a distinctly lower T than preceding events (35 s as compared to 37-40 s), and is the last event conduit-reservoir event recorded in our catalog. This event started with an impulsive inflation, though with minimal broadband energy. Another larger broadband impulse occurred a minute later that corresponded to increased oscillation amplitude, after which the oscillation decayed exponentially.

3.1.1 Conduit-reservoir resonance

The first category of signals we term 'conduit-reservoir modes' *Liang et al.* [2019a]. These modes constitute the main trend of VLPs starting at T ~20 s in 2010, increasing to ~40 s in early 2011, and fluctuating between 35-43 s from 2012 until the caldera collapse onset in May 2018 (Fig. 13, 14). Some other signals prior to 2010 and during the series of lava-lake draining events in 2011 may also fit into this category.

The conduit-reservoir oscillation is the fundamental resonant mode of the coupled conduit and shallow magma reservoir system, in which the magma column in the conduit oscillates vertically and pushes magma in and out of the underlying reservoir [*Liang* *et al.*, 2019b]. Other resonant modes such as Krauklis (crack) waves or acoustic resonance are predicted to generally have higher frequencies and lower amplitudes [*Karlstrom et al.*, 2016; *Liang et al.*, 2019a]. Restoring forces for the conduit-reservoir oscillation come from magma reservoir compressibility (combined wall rock elasticity and multiphase magma compressibility) and gravity [*Liang et al.*, 2019a]. Viscous drag along the conduit walls is probably the primary control of damping for these oscillations, and also impacts resonant period. Ground deformation during these events is primarily from uniform inflation/deflation of the magma reservoir; deformation from the conduit is small by comparison [*Liang et al.*, 2019b].

Conduit-reservoir mode resonance could be triggered/driven by a variety of different mechanisms, producing signals with different onset characteristics. We term conduit-reservoir modes with abrupt onsets and inflationary first motions 'Normal' events; this category includes rockfall or lava-lake surface explosion triggered events and is analogous to 'type 2' events in [*Dawson et al.*, 2014]. There is often high-frequency or broadband energy present at the onset of Normal events, as well as inflationary steps in tilt data [*Chouet et al.*, 2013; *Orr et al.*, 2013; *Dawson et al.*, 2014] (Fig. 11, 12, S.23, S.24). We term conduit reservoir modes with abrupt onsets and deflationary first motions 'Reverse' modes; analogous to 'type 3' events in [*Dawson et al.*, 2014] (Fig. 11). These signals often do not have obvious high frequency triggers, and some exhibit deflationary tilt steps [*Dawson et al.*, 2014]. The trigger for Reverse events is not known [*Dawson et al.*, 2014], but could involve impulsive mass injections at depth or bubble rise/collapse. Some conduit-reservoir events do not fit very clearly into either category, for example those with gradual onsets or multiple step increases in oscillation amplitude (Fig. 12, S.24).

Our algorithm classifies ~77% of conduit-reservoir events after 2012 as Normal, ~17% as Reverse, and the remaining ~6% are undetermined (Fig. 16). Prior to 2012 our classifications are less reliable due to the prevalence of VLP tremor and shorter resonant periods (which makes phase offsets between stations less negligible). The mean and median amplitudes of Normal events are both about twice as large as those of Reverse events, though both types of events exhibit variation in amplitude over orders of magnitude (Fig. S.13). We do not find any appreciable differences in distributions of T or Q between Normal and Reverse events, and also do not find any appreciably different correlations against other datasets (such as tilt or lava-lake elevation) between the two types of events (Fig. S.13).

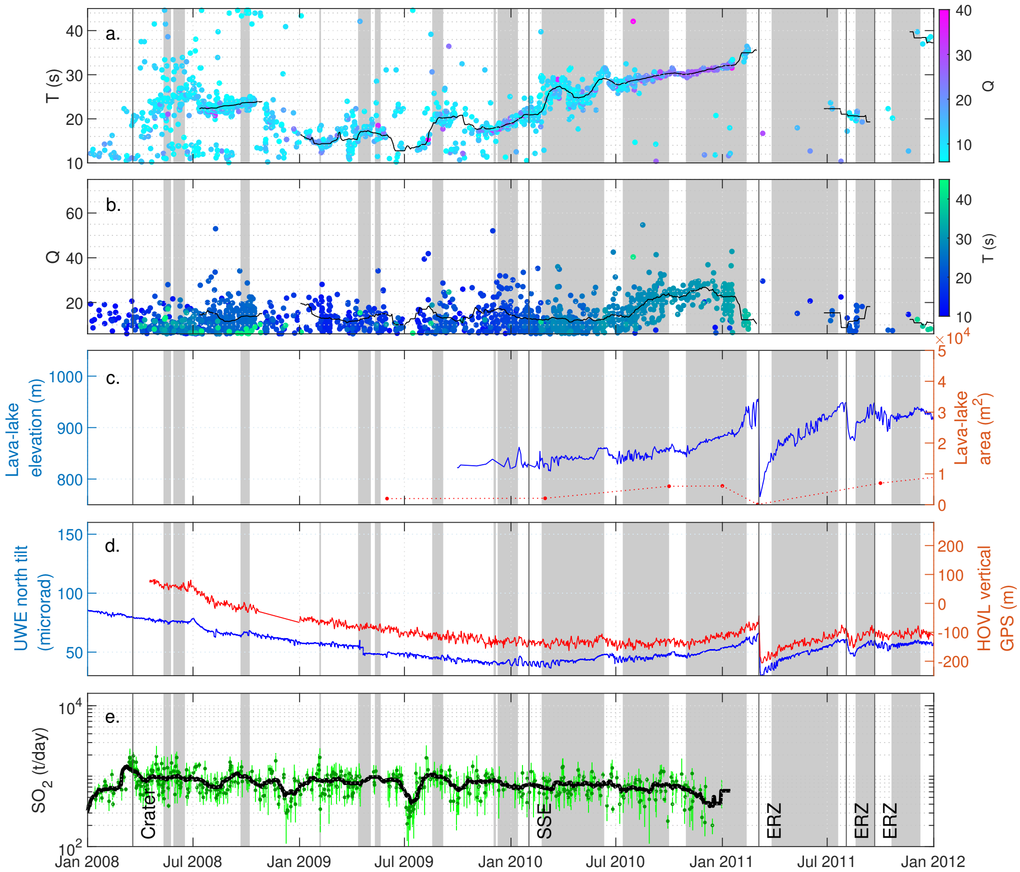

Figure 13. Section of the VLP catalog from 2008-2011. Black lines in the plots a and b show 30-day moving averages over the modes we have labeled as potential conduit-reservoir modes, neglecting outliers or events from times with no consistent dominant period. In plot e dark green dots indicate average daily SO_2, light green lines indicates standard deviations, and the black line is a 30-day moving average. 'Crater' indicates where the Halemaʻumaʻu crater first formed, 'SSE' indicates slow slip events, 'Int' indicates documented summit intrusions, and 'ERZ' indicates eruptions along the East-Rift-Zone. Grey bars in all plots indicate times of long-term ground inflation (Section 2.8).

3.1.2 Lava-lake sloshing

The second category of signals we term 'lava-lake-sloshing modes' *Dawson et al.* [2014]; *Liang and Dunham* [2020]. These have T of 10-20 s, and are recognizable from 2010-2018 in our catalog (Fig. 13, 14).

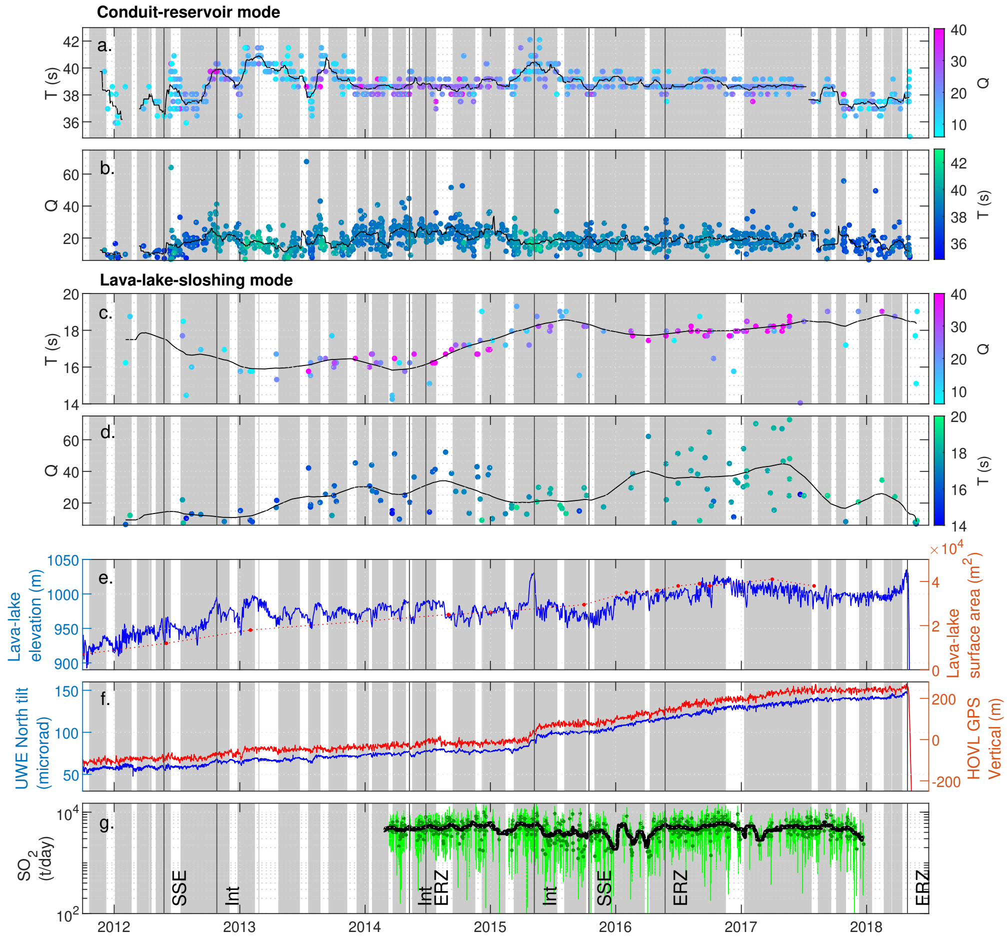

Figure 14. Section of the VLP catalog highlighting conduit-reservoir and lava-lake-sloshing resonance from 2012-2018. Black lines in plots a and b show 30-day moving averages, and in plots c and d show 120 day moving averages. ‘SSE’ indicates slow slip events, ‘Int’ indicates documented summit intrusions, and ‘ERZ’ indicates eruptions along the East-Rift-Zone. Grey bars in all plots indicate times of long-term ground inflation (Section 2.8).

Modeling/inversions for select examples of lava-lake-sloshing events [*Liang and Dunham*, 2020] supports earlier suggestions [*Dawson et al.*, 2014] that they are likely caused by lateral surface gravity wave resonance in the lava-lake (i.e., ‘sloshing’). The resulting pressure perturbations at the top of the conduit may also force magma flow down the conduit causing a forced oscillation in the conduit-reservoir system [*Liang and Dunham*, 2020].

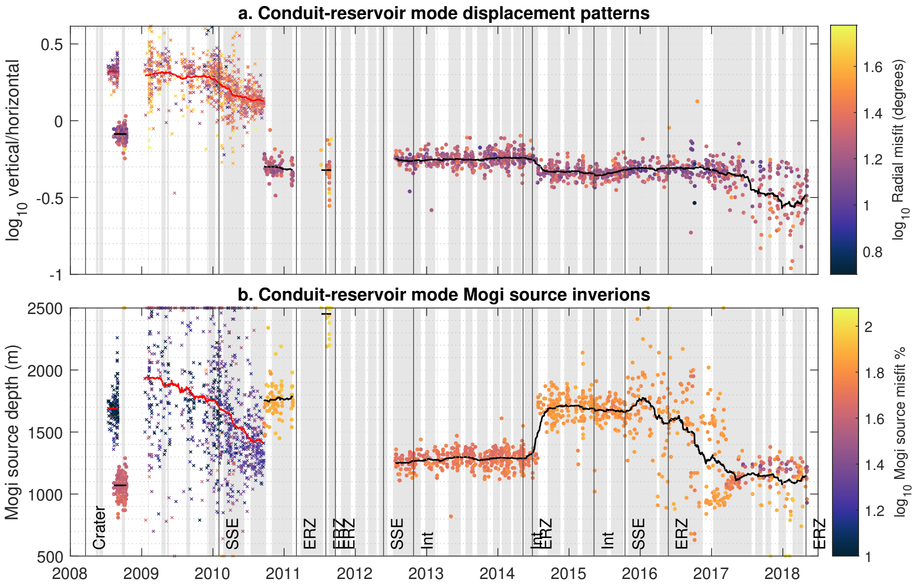

536 **Figure 15.** Ground displacement patterns and Mogi spherical reservoir source inversions for conduit-reservoir modes. Dots and black lines indicate events and 120-day moving averages for times with more than 6 stations available. Crosses and red lines indicate events and 120-day moving averages for times with only one station available, so ground displacement patterns are poorly constrained and should not be directly compared to events with more stations. Depths are relative to the caldera floor. 'Crater' indicates where the Halema'uma'u crater first formed, 'SSE' indicates slow slip events, 'Int' indicates documented summit intrusions, and 'ERZ' indicates eruptions along the East-Rift-Zone. Grey bars in all plots indicate times of long-term ground inflation (Section 2.8).

Around 75% of these modes appear alongside Normal conduit-reservoir modes; the rest appear in isolation (Fig. 11, 12, 16, S.22, S.24). We found no examples occurring alongside Reverse modes. There are some times where at least two distinct lava-lake-sloshing modes occur (Fig. 12, S.24); likely representing sloshing in different directions with an irregular lava-lake geometry [*Liang and Dunham*, 2020]. These do not appear to be very prevalent in our catalog, though such modes with low signal/noise ratio or very close period to a larger lava-lake-sloshing mode may have been missed.

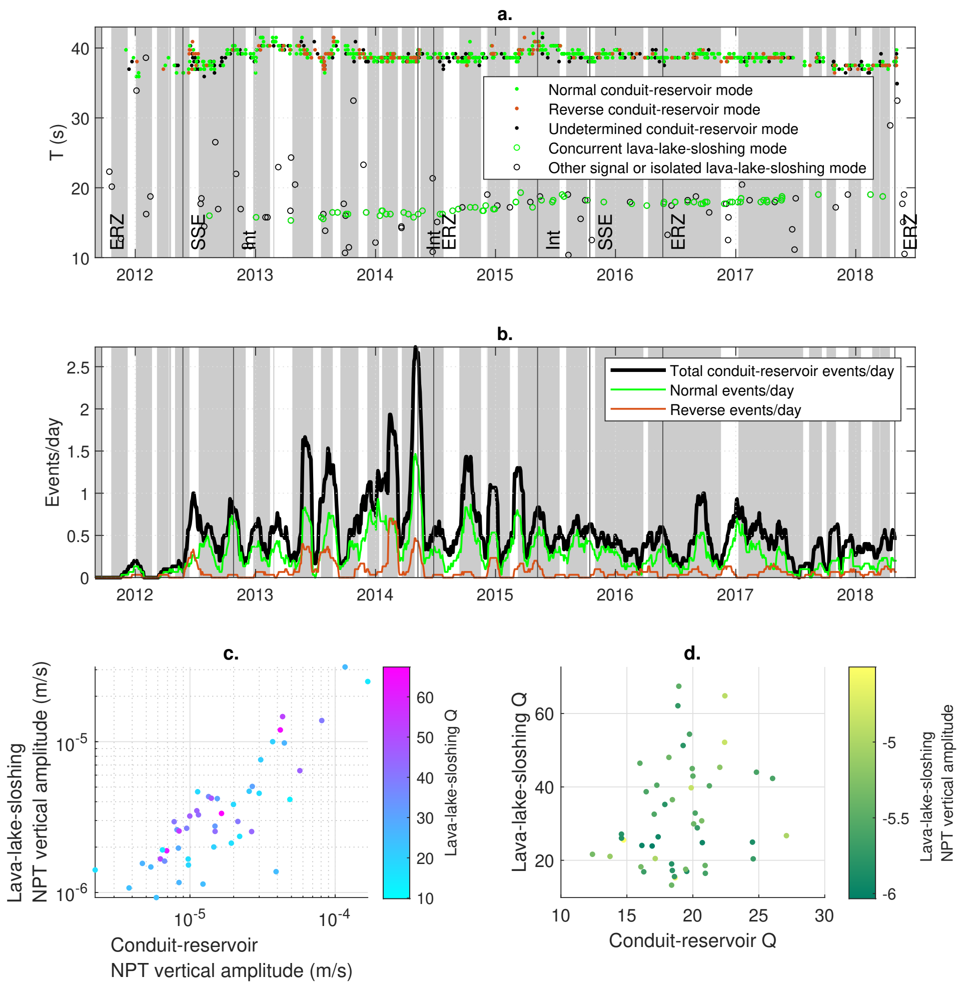

Figure 16. Plot a shows the onset polarity (Normal or Reverse) of conduit-reservoir events, and lava-lake-sloshing modes that occurred alongside a detected conduit-reservoir event. Plot b shows conduit-reservoir event density calculated over 30-day windows. We note that event density will vary by orders-of-magnitude depending upon the event detection thresholds used (Section 2.5), so is most useful for comparing relative event densities through time. ‘Crater’ indicates where the Halema‘uma‘u crater first formed, ‘SSE’ indicates slow slip events, ‘Int’ indicates documented summit intrusions, and ‘ERZ’ indicates eruptions along the East-Rift-Zone. Grey bars in plots a and b indicate times of long-term ground inflation (Section 2.8). Plot c compares amplitudes (from vertical velocity at station NPT) of conduit-reservoir modes with corresponding lava-lake-sloshing modes. Plot d compares Q of conduit-reservoir modes with corresponding lava-lake-sloshing modes.

3.1.3 VLP tremor

We use the term 'VLP tremor' to refer to signals with clearly elevated energy in one or more relatively focused periods, but that are not obviously isolated in time and lack clear onsets and/or exponential decays. These signals occur throughout the study timespan (Fig. 11, S.15, S.16, S.17, S.18, S.19, S.21).

Many of these signals have the same dominant periods as nearby impulsively-triggered conduit-reservoir or lava-lake-sloshing modes. We therefore hypothesize that they represent the same resonant modes with more continuous rather than discrete forcing. Continuous forcing could occur via superposition of discrete impulses such as rockfalls [*Orr et al.*, 2013], surface explosions/bubble bursts [*Chouet et al.*, 2010; *Richardson and Waite*, 2013], or rock fracture/slip [*Aki et al.*, 1977; *Chouet*, 1996]. Continuous tremor has also been hypothesized to arise from magma flow through irregular channels [*Julian*, 1994], bubble-cloud oscillations [*Matoza et al.*, 2010; *Unglert and Jellinek*, 2015], or turbulence [*Hellweg*, 2000; *Unglert and Jellinek*, 2015].

If VLP tremor amplitude is constant our method will not detect it. However, in this dataset VLP tremor amplitude is almost always variable on timescales ranging from seconds-minutes, in which case our method detects events corresponding to local maxima. Q of such signals could be controlled by the forcing time-function rather than damping of the initial resonance, so may not be sensitive to the same magma system properties as Q of impulsive-onset decaying resonant signals.

3.1.4 Gliding-frequency VLP signals

We use the term 'gliding-frequency' to refer to VLP signals with dominant periods that change over the duration of a single event (over timescales from seconds to tens of minutes). These signals are present at various times and with various starting and ending periods throughout the studied timespan (Fig. 12, S.18, S.20). While not designed to categorize gliding-frequency VLP signals, our method does detect a multitude of them.

We are not aware aware of any published analysis of these signals at Kīlauea, though gliding in higher-frequency tremor has been previously identified [*Unglert and Jellinek*, 2015]. In some cases the gliding-frequency VLP signals appear to start or end at similar periods to nearby non-gliding conduit-reservoir or lava-lake-sloshing resonances, indicating that at least some of the gliding-frequency signals may be related to these other modes.

Some gliding-frequency VLP signals may represent rising bubble slugs, which could create a varying oscillation period during ascent and then possibly trigger standard decaying conduit-reservoir resonance after bursting at the surface [*James et al.*, 2008; *Chouet et al.*, 2010]. Alternately, some gliding-frequency VLP signals may represent examples of either conduit-reservoir or lava-lake-sloshing resonance where magma properties change over the course of the resonance. This could occur if the perturbation that induces resonance destabilises some aspect of the shallow magma system, such as by causing collapse of a foam layer in the lava-lake, or by causing release and upward movement of a bubble slug or cloud.

3.2 Timeline of Kīlauea VLP Seismicity

Here we present a brief chronological overview of Kīlauea activity and VLP seismicity from 2008-2018. We break the timeline into one or two year long time-segments based on where notable changes in VLP seismicity occur.

3.2.1 January 2008-January 2010: Overlook Crater formation and intermittent lava-lake

The Overlook Crater first began forming inside the Halema'uma'u summit crater in March 2008, following months of elevated SO_2 emissions and seismicity [*Patrick et al.*, 2011; *Dawson et al.*, 2014; *Patrick et al.*, 2019b]. Two years of elevated siesmicity, long-term ground deflation, and occasional explosive events led to the establishment of a persistent lava-lake in early 2010 [*Patrick et al.*, 2011; *Dawson et al.*, 2014; *Patrick et al.*, 2019b] (Fig. 13).

Our method finds more VLP signals in early 2008 and in 2009 than previous studies [*Dawson et al.*, 2010, 2014], defining a more continuous sequence of VLPs to outline this dynamic early phase of the summit eruption sequence (Fig. 13). Average T increased and decreased significantly multiple times during this interval, from a maximum of around 25 s in July 2008 to minima of around 13 s in February and August of 2009. While measurements of lava-lake level are limited during this time, the local minima in 2009 corresponds with low reported lava-lake levels and the local maxima around July 2008 corresponds with higher reported lava-lake levels [*Patrick et al.*, 2019b].

Much of the VLP seismicity during this time was tremor (Fig. S.15, S.17), though there were times where discrete events were apparent (Fig. S.14, S.16) [*Chouet et al.*, 2011; *Dawson et al.*, 2014; *Liang et al.*, 2019b]. Q was mostly less than 20.

3.2.2 January 2010-March 2011 Kamoamoa fissure eruption: inflation and lava-lake filling

A more continuous trend of conduit-reservoir events began in November 2009 and continued until the March 2011 Kamoamoa fissure eruption (Fig. 13) [*Dawson et al.*, 2014]. In early 2010 the lava-lake became persistent and filled from an elevation of 820 m to 950 m by early 2011 [*Patrick et al.*, 2019b] (Fig. 13). The previous trend of long-term ground deflation began transitioning to gradual inflation around early 2010, and began inflating more rapidly around November 2010 (Fig. 13).

More distinct VLP events with clear impulsive onsets and decays began occurring during this time, though VLP tremor was also still present (Fig. 11) [*Chouet et al.*, 2011; *Dawson et al.*, 2014]. The discrete events were primarily Normal conduit-reservoir modes. During this time-segment a few likely lava-lake-sloshing modes began to appear alongside some of the Normal conduit-reservoir modes, with T from 10-20 s (Fig. 11, 13).

The general trend of increasing conduit-reservoir T over this time was similar to that previously identified [*Dawson et al.*, 2014], though we find more events in mid-late 2010 that help resolve two pronounced month-long spikes in T; both are about 2 s above the background trend in T. The onset of the first spike (in March 2010) corresponded to a very subtle shift from ground deflation to inflation, and was followed by a slight rise (by ~20%) in average SO_2 emissions. The second spike (in June 2010) corresponded to a pronounced local maxima in ground inflation, local maxima (~20 m above the background) in lava-lake elevation, and was followed by a slight decrease (by ~20%) in SO_2 emissions. For the remainder of this time-segment, conduit-reservoir mode T was well correlated with both ground inflation and lava-lake elevation. There was a gradual increase in Q starting around August 2010, followed by a rapid drop around February 2011 and leading up to the March 2011 Kamoamoa fissure eruption. This general trend is present in the previous Kīlauea VLP catalog [*Dawson et al.*, 2014], but the lower scatter in Q in our catalog reveals that Q was correlated with T, ground inflation, and lava-lake elevation in mid 2010 then becomes anti-correlated with all three datasets by late 2010.

Resolution of ground displacement patterns is very limited during this time-segment due to sparse station coverage. There was a continuous decrease in vertical/horizontal velocity ratios and Mogi source depths from early-mid 2010 (Fig. 15), though the velocity ratios are likely at least partially influenced by the increasing T, which will cause an apparent increase in horizontal motion due to instrument tilt [*Maeda et al.*, 2011].

3.2.3 March 2011 Kamoamoa fissure eruption-September 2011 Pu'u 'Ō'ō eruption: multiple East-Rift-Zone eruption and lava-lake draining events

After the March 2011 Kamoamoa fissure eruption, there was a gradual increase in lava-lake elevation and ground inflation leading up to the August 2011 Pu'u 'Ō'ō eruption, followed by another short stretch of ground inflation and lava-lake refilling before the September 2011 Pu'u 'Ō'ō eruption (Fig. 13). We do not detect appreciable amounts of VLP seismicity between the March 2011 Kamoamoa and August 2011 Pu'u 'Ō'ō eruptions, despite the lava-lake refilling to pre-eruption levels, though there were a couple of VLP events that exhibited strong glides in period. There was a cluster of low Q VLP activity with T around 20 s between the August and September 2011 Pu'u 'Ō'ō eruptions, including some events that exhibited strong glides in period (Fig. S.18).

3.2.4 September 2011 Pu'u 'Ō'ō eruption-October 2012 intrusion: lava-lake filling and reappearance of conduit-reservoir resonance

Until around the time of the May 2012 SSE, conduit reservoir mode resonance had very low Q, often below our detection threshold (Section 2.3), which contributes to the apparent sparsity of events (Fig. 14). During this time average lava-lake level increased from ~930 m to ~960 m, although there was only a very slight net ground inflation. After the May 2012 SSE (which also corresponds with a temporary 10-day drop in lava-lake elevation) average conduit-reservoir mode T, lava-lake elevation, and ground inflation all decreased until around August, then all continually increased until the October 2012 intrusion. Average conduit-reservoir mode Q continually increased following the SSE.

Conduit-reservoir seismicity during this time consisted of Normal and Reverse events (Fig. 11), VLP tremor (Fig. S.19), and gliding-frequency events (Fig. S.20). Analysis of conduit-reservoir mode ground displacement patterns over this time is limited by sparse station coverage. Lava-lake-sloshing modes were sparse during this time-segment so it is difficult to determine if any robust trends are present (Fig. 14).

3.2.5 October 2012 intrusion-June 2014 Puʻu ʻŌʻō eruption: stable lava-lake

Between the October 2012 intrusion and the June 2014 Puʻu ʻŌʻō eruption there was a long-term ground inflation trend, though average lava-lake level remained fairly constant (Fig. 14). The May 2014 intrusion corresponded to a step ground deflation and drop in lava-lake elevation. Within this time-segment lava-lake elevation and ground inflation were generally well correlated (Fig. 18).

Conduit-reservoir average event density ranged from 0.2-2.6 events/day during this time-segment (Fig. 16). Local maxima in event density occurred in May 2013, August 2013, February 2014, and the highest recorded event density in the post-2012 timespan occurs at the May 2014 intrusion. Conduit-reservoir T was positively correlated with lava-lake elevation and ground inflation until mid 2013 when the correlation became inconsistent, and then negative in the months leading up to the June 2014 eruption (Fig. 18). Conduit-reservoir Q was positively correlated with T, lava-lake elevation, and ground inflation in late 2012, but then was inconsistent for most of the rest of the time-segment and negatively correlated with T in the months leading up to the June 2014 Puʻu ʻŌʻō eruption. Ground displacement patterns from the conduit-reservoir modes were consistent over this time-segment (Fig. 15).

Lava-lake-sloshing events were sparse until around mid 2013. Average lava-lake-sloshing T was relatively constant, mostly between 15.5-16.5 s. Q was highly variable between 6-50, but increased on average over this time-segment (Fig. 14).

3.2.6 June 2014 Puʻu ʻŌʻō eruption-May 2016 Puʻu ʻŌʻō eruption: changed conduit-reservoir ground displacement patterns

After the June 2014 Puʻu ʻŌʻō eruption there was an abrupt change in conduit-reservoir mode ground displacement patterns, which then remained stable until around the October 2015 SSE (Fig. 15). There was fairly steady long-term ground inflation during this time-segment, with more rapid ground inflation in the months around the May 2015 intrusion, [*Patrick et al.*, 2019b] (Fig. 14). Long-term averaged lava-lake level remained fairly constant through most of this time-segment, with the exception of an overflow in the month leading up to the May 2015 intrusion, and then a more steady increase between October-December 2015. The months after the May 2015 intrusion are unique within the studied timespan for exhibiting a strong anti-correlation between lava-lake elevation and ground inflation. SO_2 emissions averaged around 5000-6000 t/day from 2014 until the May 2015 intrusion, then dropped to around 4000 t/day and remained around this level until increasing in the months leading up to the May 2016 Puʻu ʻŌʻō eruption 14).

Conduit-reservoir event density varied from 0.1-1.5 events/day during this time-segment (Fig. 16). Local maxima in event density occurred during the May 2015 intrusion, May 2016 Puʻu ʻŌʻō eruption, and generally near the onset of long-term inflation periods (for example October 2014, December 2014, and March 2015). Conduit-reservoir *T* was remarkably constant around 39 s, until increasing to 41 s in the months leading up to the May 2015 intrusion, after which it decreased for the remainder of the timespan (Fig. 14). There was a local minima in *T* corresponding to the October 2015 SSE. *T* was fairly well correlated with lava-lake elevation and ground inflation, except in the months following the June 2014 eruption (Fig. 18). Conduit-reservoir *Q* averaged around 25 until a few months before the May 2015 intrusion, when it dropped to around 18 and remained stable for the remainder of the time-segment. *Q* was mostly anti-correlated with *T* during this time-segment, and not strongly correlated to lava-lake elevation or ground inflation.

Lava-lake-sloshing *T* increased steadily until a few months after the May 2015 intrusion, then decreased until early 2016, then again increased more gradually for the remainder of the time-segment (Fig. 14). Lava-lake-sloshing *T* or *Q* did not appear to correlate with any of the other datasets during this time.

3.2.7 May 2016 Puʻu ʻŌʻō eruption-May 2018 caldera collapse onset: variable conduit-reservoir ground displacement patterns and climactic eruption precursors

The months around the May 2016 Puʻu ʻŌʻō eruption heralded a net change in VLP ground displacement patterns, albeit with significant scatter (Fig. 15). Ground displacement patterns then remained consistent until the May 2018 caldera collapse onset. Long-term averaged lava-lake elevation increased until late 2016 when small overflows occurred [*Patrick et al.*, 2019b], then decreased until mid 2017, then remained stable until it began increasing steeply in March 2018 and eventually overflowed on April 26, then began draining on May 2 [*Neal et al.*, 2019] (Fig. 14). There was consistent long term ground inflation until mid 2017, then little net inflation or deflation until consistent inflation began again around March 2018. Lava-lake elevation and ground inflation were mostly correlated during this time-segment, with the exception of a few months in mid 2017 (Fig. 18). After the May 2016 Puʻu ʻŌʻō eruption SO_2 emissions stabilize at around 5000 t/day, and remained at this level except for drops in early 2017 and late 2017 (when the published data ends).

Conduit-reservoir event density varied from 0-1 events/day during this time-segment (Fig. 16). decreased in the months following the May 2016 Puʻu ʻŌʻō eruption, exhibited local maxima in September 2016 and January-May 2017, and remained relatively stable in the year leading up to the 2018 caldera collapse. Conduit-reservoir mode T was stable around 39 s until October 2017 when it dropped to 37 s; then increased again in the months leading up to the May 2018 collapse eruptions (Fig. 14). During this time-segment T was alternately correlated and anti-correlated with lava-lake elevation and ground inflation (Fig. 18). Conduit-reservoir mode Q remained around 18 until August 2017, when it became more variable for the remainder of the time-segment. Q was anti-correlated with T until late 2017, and was alternately correlated and anti-correlated with lava-lake elevation and ground inflation.

Lava-lake-sloshing modes were numerous until around May 2017, then sparse during the rest of the time-segment (Fig. 14). Lava-lake-sloshing T increased fairly steadily, except for a decrease in May 2018. Lava-lake-sloshing Q was highly variable during this time-segment.

3.3 General correlations among datasets

Here we analyze correlations between the various geodetic datasets, conduit-reservoir resonant properties, and lava-lake sloshing properties.

3.3.1 Correlations among geodetic datasets

Ground surface deformation data from near field tilt-meters and GPS stations indicates the rate of ground inflation/deflation of the Kīlauea summit region. This primarily reflects pressure in the shallow summit reservoir, but may also be influenced by pressure

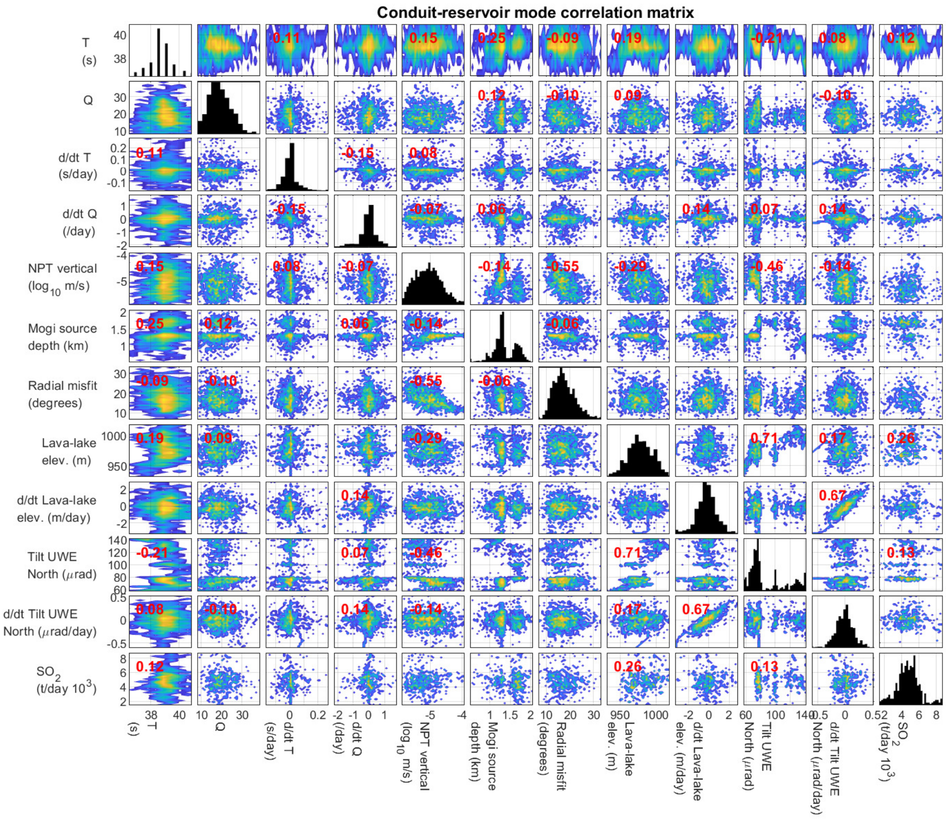

Figure 17. Conduit-reservoir mode correlation matrices from 2012-2018 (see Fig. S.12 for the full 2008-2018 timespan). Off-diagonal plots are colored by the logarithm of the number of points in a given parameter bin, and histograms on diagonal plots show the distribution of each parameter. Red numbers are Pearson's correlation coefficients, only shown for correlations with P-values less than 0.05. 'Lake h' indicates lava-lake elevation. All time derivatives, notated by 'd/dt', were calculated with a 7-day cutoff-period differentiator filter (Section 2.8).

in the proposed deeper south caldera reservoir [*Baker and Amelung*, 2012; *Anderson et al.*, 2015; *Anderson and Poland*, 2016; *Anderson et al.*, 2019] or along the ERZ [*Montagna and Gonnermann*, 2013].

Lava-lake elevation is generally positively correlated with ground inflation, particularly on timescales of months or less, as captured by moving correlations (Fig. 18) and correlations between time derivatives (Fig. 17, S.12). These timescales include the prevalent deflation-inflation (DI) events [*Patrick et al.*, 2016a,b; *Anderson et al.*, 2019]. This correlation implies that lava-lake elevation is analogous to a Pitot tube for the summit magma reservoir, where the exact relation between lava-lake level and reservoir pres-

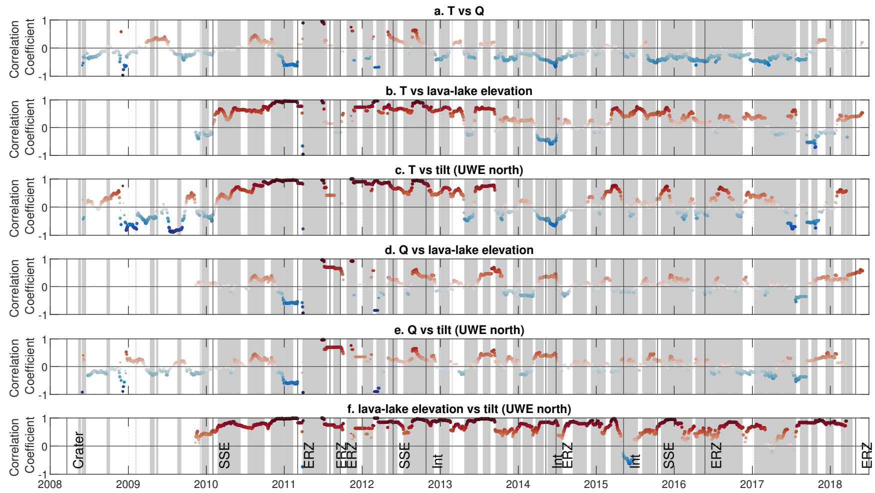

Figure 18. Conduit-reservoir mode Pearson's correlation coefficients calculated over moving 90-day windows. Windows with less than 4 data points were excluded. Larger dots indicate lower p-values; the largest dot size (encompassing ~30-70% of the values in each plot) corresponds to p-values less than 0.05. 'SSE' indicates slow slip events, 'Int' indicates documented summit intrusions, and 'ERZ' indicates eruptions along the East-Rift-Zone. Grey bars in the all plots indicate times of long-term ground inflation (Section 2.8).

sure will depend on reservoir stiffness and on the magma density profile [*Patrick et al.*, 2015; *Anderson et al.*, 2015, 2019]. However, there are isolated times where this correlation breaks down (Fig. 14, 18). Additionally, the correlation between ground inflation and lava-lake elevation over the whole timespan exhibits strong scatter (Fig. 17, S.12), indicating that the relation between ground inflation and lava-lake elevation is not constant over time. This is partly caused by gradual long-term changes, such as in early 2017 when ground inflation and lava-lake elevation are positively correlated on day-week timescales but long-term lava-lake level remains constant despite long-term ground inflation (Fig. 14). There are also abrupt events that change the relation between ground inflation and lava-lake elevation, such as the May 2015 intrusion (Fig. 14).

There was typically an increase in lava-lake elevation and ground inflation over days-months leading up to ERZ eruptions, followed by an abrupt ground deflation and decrease in lava-lake elevation (Fig. 14). The exception was the June 2014 Pu'u 'Ō'ō eruption, around which there were no significant changes in lava-lake elevation or ground inflation. Among ERZ eruptions, SO_2 data is only available around the June 2014 and May

2016 Pu'u 'Ō'ō eruptions, but there did appear to be an increase in SO_2 emissions by approximately a factor of 2 over the months leading up to the May 2016 Pu'u 'Ō'ō eruption (Fig. 14).

There was also typically an increase in lava-lake elevation and ground inflation over days-months leading up to intrusions, followed by an abrupt ground deflation and decrease in lava-lake elevation (Fig. 14). However, the ground deflation following intrusions was much less pronounced than the drops in lava-lake elevation. SO_2 data is only available around the May 2014 and May 2015 intrusions, but there did appear to be a decrease in SO_2 emissions by approximately a factor of 1.5 in the months following the May 2015 intrusion (Fig. 14).

Some slow-slip events (SSEs), where aseismic slip on a fault occurs over timescales of hours-days [*Schwartz and Rokosky*, 2007], have been linked to magmatic activity such as diking events at Kīlauea [*Brooks et al.*, 2008; *Montgomery-brown et al.*, 2015]. The January 2010 and October 2015 SSE do not appear to correspond to changes in lava-lake elevation, ground inflation, or SO_2 emissions (Fig. 13). The May 2012 SSE does correspond to a several day drop in lava-lake elevation and ground inflation (Fig. 14).

3.3.2 Conduit-reservoir resonance correlations

During most of the timespan conduit-reservoir mode T and Q exhibit a weak negative correlation, with an overall Pearson's correlation coefficient of -0.06 but local correlation coefficients often around -0.7 (Fig. 17, 18, S.12). There are isolated times where T and Q are positively correlated, such as in mid 2010 (correlation coefficient near 1) and mid 2012 (correlation coefficient around 0.7) (Fig. 13, 14, 18).

Conduit-reservoir mode T is positively correlated with lava-lake elevation during most of the timespan, with correlation coefficients mostly between 0.3 and 1 (Fig. 18), and a weak overall correlation coefficient of 0.11 (Fig. 17, S.12). However, there are some times with negative local correlations, such as around the 2014 Pu'u 'Ō'ō eruption (correlation coefficient around -0.6), and in late 2017 (correlation coefficient around -0.7). The correlation between T and ground inflation (i.e., tilt) exhibits a similar trend to the correlation between T and lava-lake elevation after the arrival of a persistent lava-lake in late 2009, and exhibits a variable but mostly negative trend prior to this (Fig. 17, 18, S.12).

Conduit-reservoir T is positively correlated with event amplitude, even when considering only vertical velocity (which should not be sensitive to instrument tilt) (Fig. 17, S.12).

We find increases in both conduit-reservoir event density and T around the documented October 2012 and May 2015 intrusions. There is no obvious change in Q corresponding to either intrusion, though the the correlation between T and Q does change from positive to negative at the October 2012 intrusion (Fig. 7, 18). Neither intrusion appears to correspond to changes in ground displacement patterns (Fig. 15).

ERZ eruptions for which we detect conduit-reservoir modes both before and after the events (i.e., the June 2014 and May 2016 Pu‘u ‘Ō‘ō eruptions) don't obviously relate to changes in conduit-reservoir mode T or Q. However, sharp changes in the correlations between T and Q, T and lava-lake elevation/tilt, and Q and lava-lake elevation/tilt occur alongside the June 2014 eruption, and more subtle changes in these correlations may also be present alongside the May 2016 eruption (Fig. 7, 18). There are pronounced changes in ground displacement patterns following both eruptions that are readily apparent in the time-series of Mogi source inversions and vertical/horizontal velocity ratios (Fig. 15). There is an apparent increase in Mogi source centroid depth following June 2014, and then an apparent decrease following May 2016 (though with more scatter in the inverted depths around this time).

3.3.3 Lava-lake-sloshing correlations

Due to the smaller amount of lava-lake-sloshing modes present it is more difficult to determine whether lava-lake-sloshing T or Q are correlated with other datasets. Long-term average lava-lake-sloshing T increased over most of the timespan, with the exception of 2012 when lava-lake sloshing events were sparse and exhibited large scatter in T. The long-term increase in T roughly corresponds to an observed long-term increase in lava-lake surface area [*Patrick et al.*, 2019b]. There is appreciable scatter (of about 3 s) in T on timescales of months or less; though much of this appears to be due to a small number of outlier events. Lava-lake-sloshing Q exhibits large scatter over most of the timespan, with the exception of 2012 when Q was generally less than 20, and 2015 when Q was generally between 10 and 30 (corresponding to a local maxima in lava-lake-sloshing T).

There is a roughly linear relation between conduit-reservoir mode amplitude and lava-lake-sloshing mode amplitude, though with an appreciable amount of scatter (Fig.

16). Lava-lake-sloshing Q does not appear to be correlated with conduit-reservoir mode Q (Fig. 16).

4 Discussion

Very-Long-Period seismic events in our new catalog provide an outstanding tool both to document the progression of a long-lived (10 year) open vent eruptive episode at Kīlauea Volcano and probe shallow magma plumbing system geometry and magma properties through time. In the following discussion we provide a conceptual modeling framework for understanding the physical origin of observations documented in previous sections, based largely on previously published work. We leave a detailed inversion of these events and true uncertainty quantification for future studies.

4.1 Interpreting changes in conduit-reservoir resonance

The conduit-reservoir mode is the most common and also most variable class of VLP events in our catalog. The reduced conduit-reservoir mode model of *Liang et al.* [2019a] provides estimates of T and Q assuming a cylindrical conduit and isothermal conditions, neglecting inertia and viscous drag in the overlying lava-lake and compressibility of magma in the conduit. The inviscid conduit-reservoir resonance period is [*Liang et al.*, 2019a]:

$$T_0 = 2\pi\sqrt{\frac{L_c\bar{\rho}_c}{\Delta\rho_c g\sin\alpha + A_c C_t^{-1}}}. \tag{9}$$

where L_c is conduit length, $\bar{\rho}_c$ is average magma density in the conduit, $\Delta\rho_c$ is density difference between the bottom and top of the conduit, α is conduit dip angle, A_c is conduit cross-sectional area, and C_t is total reservoir storativity:

$$C_t = (\kappa_m + \kappa_{res})V \tag{10}$$

where κ_m and κ_{res} are magma and reservoir compressibility ($\frac{3}{4G}$ for a spherical reservoir [*McTigue*, 1987]) and V is reservoir volume. With viscous damping included, T and Q depend upon T_0 as well as a momentum diffusion timescale:

$$\tau_{visc} = \frac{R_c^2\bar{\rho}_c}{\mu_c}, \tag{11}$$

where R_c is conduit radius and μ_c is average magma viscosity (Fig. 19).

We can use this model to estimate the parameter variation that could cause observed variation in T and Q (Fig. 19). We focus on short timescales (days-weeks), for which it is

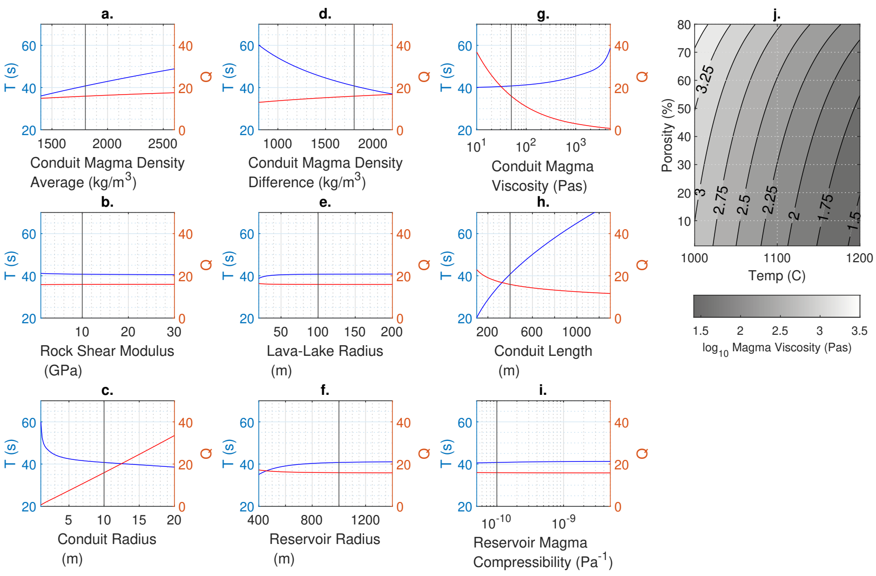

Figure 19. Plots a-i show predicted variation in T and Q due to varying each model parameter in isolation in the reduced conduit-reservoir resonance model of *Liang et al.* [2019a] (Eq. 9-11), assuming a spherical reservoir geometry. Black lines indicate the default value used for each parameter. Plot j shows apparent magma viscosity as a function of temperature and porosity (Section 4.1).

reasonable to assume that the geometry of the system remains constant. Parameters most likely to cause variation in T and Q on short timescales are properties of the multiphase magma contained within the conduit-reservoir system: average magma density, density difference, and apparent viscosity (magma compressibility probably has a comparatively minimal influence, see Fig. 19). Figure 19 shows that of these magma properties, T is most sensitive to average magma density and magma density difference. Variation in either parameter of up to ~500 kg/m^3 would be required to explain the observed short-term variability in T of up to ~6 s (Fig. 14). Q is most sensitive to magma viscosity (Fig. 19). Variation in magma viscosity of up to an order of magnitude would be required to explain the observed short-term variability in Q of up to an order of magnitude (Fig. 14, 19). It is interesting to note that none of the model parameters changing in isolation would produce a positive correlation between T and Q, as is sometimes observed (Fig. 18).

Variation in apparent magma viscosity could be partly due to changing bubble number and/or size distributions [*Manga and Loewenberg*, 2001; *Pal*, 2003; *Llewellin and Manga*, 2005; *Huber et al.*, 2014] (Fig. 19). Basaltic melt viscosity will also change slightly with dissolved volatile contents, and strongly with temperature [*Giordano et al.*, 2008] (Fig. 19). We show how magma viscosity might vary in response to temperatures and porosity in Figure 19 (plot j). Melt viscosity is obtained from the model of *Giordano et al.* [2008], using the average Kīlauea glass composition from *Edmonds et al.* [2013] and dissolved H_2O and CO_2 contents from the solubility model of *Burgisser et al.* [2008], assuming a pressure of 19 MPa. Apparent magma (melt + bubbles) viscosity is then obtained by using the low capillary-number model from *Llewellin and Manga* [2005]):

$$\mu = (1 - \phi)^{-1} \mu_l \tag{12}$$

where μ_l is melt viscosity and ϕ is porosity.

Changes in melt temperature could arise due to due to changes in convective regimes [*Jones et al.*, 2006; *Witham and Llewellin*, 2006; *Harris*, 2008] or influx/recharge of deeper magma. For example, convection extending from the lava-lake surface though the conduit might result in lower average magma temperatures in the conduit than if there are separate convective cells in the lava-lake and conduit [*Patrick et al.*, 2016b].

While the model of *Liang et al.* [2019a] (outlined in Eq. 9-11) provides an excellent starting point for interpreting changes in T and Q, it involves a number of simplifications that would need to be improved to allow for a more detailed analysis of Kīlauea VLP seismicity. Chiefly, incorporating a background state model for magma density profiles, whether from a simple magmastatic case [*Karlstrom et al.*, 2016] or considering exchange flow [*Fowler and Robinson*, 2018], would be necessary to assess how average magma density and density gradient in the conduit vary with lava-lake elevation and/or reservoir pressure. This relation likely plays a role in the observed correlations between T, lava-lake elevation, and ground inflation. Inertia in the lava-lake and variations in conduit and lake geometry with depth, which are neglected in the model of *Liang et al.* [2019a] (Eq. 9-11), may affect both T and Q and also contribute to the observed correlation between T and lava-lake elevation. Lastly, a more detailed treatment of damping that includes the effects of bubbles on viscosity [*Manga and Loewenberg*, 2001; *Llewellin and Manga*, 2005; *Gonnermann and Manga*, 2013; *Huber et al.*, 2014], bubble growth and resorption [*Karlstrom et al.*, 2016], and viscous drag in the lava-lake would be necessary to accurately interpret changes in Q.

4.2 Interpreting changes in lava-lake-sloshing

The lava-lake-sloshing mode at Halemaʻumaʻu has been modeled as incompressible surface gravity wave resonance in a cylindrical or wedge-shaped tank [*Dawson et al.*, 2014; *Liang and Dunham*, 2020]. General studies of incompressible fluid sloshing in various tank geometries indicate that T and Q depend on fluid density and viscosity, tank width, and tank depth (in the case of shallow tanks) [*Bauer*, 1981; *Ibrahim*, 2005]. The period for the fundamental sloshing mode of incompressible fluid in a cylindrical tank is given by [*Ibrahim*, 2005]:

$$T = \frac{2\pi}{\sqrt{1.841\frac{g}{R_L}\tanh\left(1.841\frac{h_L}{R_L}\right)}} \tag{13}$$

where R_L is lake radius and h_L is lake depth.

Due to the presence of exsolved volatiles and a solidified surface crust [*Karlstrom and Manga*, 2006], magma in the Halemaʻumaʻu lava-lake will generally be compressible and stratified [*Carbone and Poland*, 2012; *Carbone et al.*, 2013; *Patrick et al.*, 2016a; *Poland and Carbone*, 2016]. Previous inversions [*Liang and Dunham*, 2020] suggest that the lava-lake sloshing drives magma in and out of the conduit/reservoir, so viscous dissipation from both the conduit and the lava-lake walls needs to be considered. The degree of coupling between lateral fluid motions in the lake and vertical fluid motions in the the conduit will depend on the offset of the top of the conduit along the lava-lake sloshing axis, and thus on the direction of lava-lake sloshing [*Liang and Dunham*, 2020]. The solid crust on the lava-lake surface is likely not static during VLP events, as indicated by videos of rockfall-triggered lava-lake-sloshing events where the crust sometimes disintegrates/overturns following event onsets [*Orr et al.*, 2013; *Patrick et al.*, 2014, 2016a; *USGS*]. Thus a quantitative interpretation of T and Q for lava-lake-sloshing modes would require modeling that can account for all of these factors, self-consistently coupled to the conduit-reservoir resonator. However, we can still gain some qualitative insights into the lava-lake-sloshing modes with isolated tank models.

If we focus on short timescales (days-months), we can assume that the crater geometry is constant. Lava-lake-sloshing T exhibits variability within ~3 s on short timescales (Fig. 14). Part this may be due to sloshing along different axes of the lava-lake with different diameters (Eq. 13). A correlation between lava-lake elevation and T would also be expected if lava-lake walls are inward dipping so that diameter decreases with depth. Such a correlation does not obviously appear in our catalog (Fig. 14), though this may be due to the irregular crater geometry ([*Patrick et al.*, 2019b]).

Lava-lake-sloshing Q exhibits order-of magnitude variation on short timescales (days-months) (Fig. 14). We can rule out lava-lake elevation as a sole cause of this variation in Q by noting that many events occurring at similar lava-lake elevations have very different values of Q (Fig. 14). Thus some combination of variation in lava-lake elevation, magma properties, and sloshing direction are likely responsible for observed short-timescale variation in Q.

The lack of observed correlation between Q of conduit-reservoir modes and Q of lava-lake-sloshing modes (Fig. 16) suggests that magma properties in the lava-lake and conduit are largely decoupled. Gas volume fraction increases non-linearly as a magma rises [*Gonnermann and Manga*, 2009] while solubility also decreases [*Iacono-Marziano et al.*, 2012], and the presence of a semi-solid lava-lake crust traps bubbles in the near surface. So it is likely that porosity in the lava-lake will be much higher on average than in the conduit, consistent with inferences from gravity [*Carbone and Poland*, 2012; *Carbone et al.*, 2013; *Poland and Carbone*, 2016]. If the discrepancy in viscosities between the conduit and lava-lake also requires appreciably different average melt temperatures, this would additionally suggest separate convective cells in the lava-lake and conduit [*Patrick et al.*, 2016b].

If all lava-lake-sloshing modes had the same forcing (for example rockfall) location and satisfied appropriate small-amplitude assumptions, we would expect a linear relationship between lava-lake-sloshing amplitude and conduit-reservoir mode amplitude. A roughly linear relationship is observed, though with appreciable scatter (Fig. 16). This scatter could be partly explained by variable forcing location, which might affect the amplitude of lava-lake sloshing induced by a given pressure perturbation, the coupling of lava-lake sloshing to ground displacements [*Liang and Dunham*, 2020], and/or the coupling of the pressure perturbation at the lava-lake surface to pressure at the top of the conduit, which controls conduit-reservoir mode amplitude [*Liang et al.*, 2019a,b].

5 Conclusions

We have presented a workflow for using wavelet transforms to both detect and categorize VLP seismic signals. These methods effectively detect multiple distinct spectral peaks in impulsive events and provide robust estimates of quality factors. These methods do not rely upon any training data, are fast to implement, and are readily transferable. The ability to robustly detect new types of resonant signals, in a fully automated and computationally efficient manner, makes our method potentially useful for near-real-time volcano monitoring.

We then used these methods to generate a catalog of ~3000 VLP events that occurred between 2008-2018 during a prolonged open vent eruptive episode at Kīlauea Volcano, Hawaii USA. This catalog expands upon earlier VLP catalogs by characterizing more types of signals and refined estimates of quality factors, revealing new a rich and structured timeseries of events that documents changes to the shallow magma plumbing structures and to multiphase magma properties.

We characterize changes in period, quality factor, and ground displacement patterns over timescales ranging from hours to decades for the 'conduit-reservoir' oscillation, which is prevalent over most of this timespan and represents the fundamental resonant mode of the shallow magma plumbing system. These likely indicate changes in magma properties such as density and viscosity in the conduit, and/or changes in magma plumbing system geometry over the course of the eruptive episode. Auxiliary geophysical data such as tilt, lava lake elevation, and SO_2 emissions corroborate these inferences and help place the conduit-reservoir resonant mode amongst a rich suite of existing data available to understand the 2008-2018 eruptive episode.

We also characterize a trend of secondary 'lava-lake-sloshing' resonant signals between 2010 and 2018. These exhibit a relatively consistent increase in period over time, but wide variability in quality factors. This variability likely indicates changes in lava-lake geometry, magma density, and magma viscosity. There is no strong correlation between lava-lake-sloshing and conduit-reservoir mode quality factors, suggesting some decoupling between magma properties in the conduit and lava-lake. We do not attempt to co-invert VLP modes with other data, but see this as a rich opportunity for future work on an exceptionally well documented eruptive episode at Kīlauea volcano.

A: Synthetic Waveform Tests

We construct synthetic seismograms to test the resonant signal detection and classification methods described in the methods section. Displacements are calculated from an isotropic point source in an elastic half space model [*Aki and Richards*, 1993], with the source located 1 km beneath the Halemaʻumaʻu vent. The synthetic source-time functions consist of combinations of step displacements and exponentially decaying sinusoids with impulsive onsets. We apply a sinusoidal taper to the signal onsets to prevent sharp discontinuities and create signals with continuous first derivatives (Fig. S.1). The sinusoid used as a taper has the same period as the signal, amplitude equal to the initial signal amplitude divided by $\sqrt{2}$, and is joined at the location where the derivative and position of the taper match those of the signal. Where step displacements are also added, we taper the step displacement over the same wavelength used to taper oscillation onsets (Fig. S.2). We then add white noise from a standard normal distribution, scaled to various fractions of the signal amplitude as listed in each test figure. We then calculate displacements and tilts at each station location using the point source Green's functions, and convolve these with the instrument responses [*Maeda et al.*, 2011; *Liang et al.*, 2019b].

Acronyms

AR Auto-Regressive

CWT Continuous Wavelet Transform

DFT Discrete Fourier Transform

ERZ East Rift Zone

FIR Finite Impulse Response

FWHM Full Width at Half Maximum

GPS Global Positioning

HVO Hawaiian Volcano Observatory

IIR Infinite Impulse Response

LTA Long Term Average

SSE Slow Slip Event

STA Short Term Average

STFT Short Time Fourier Transform

UV Ultra-Violet

VLP Very-Long-Period

Notation

$\boldsymbol{T}$ period

$\boldsymbol{Q}$ quality factor

$\boldsymbol{f}$ frequency

ω angular frequency

$\boldsymbol{u}$ measured ground surface displacement

$\boldsymbol{w}$ modeled ground surface displacement

$\dot{\boldsymbol{u}}$ measured ground surface velocity

$\dot{\boldsymbol{w}}$ modeled ground surface velocity

Acknowledgments

Additional figures S.1-S.24 are included in the supplement. The Kīlauea VLP seismicity catalog is available at *(included as a spreadsheet with this submission, and will also be uploaded to a data repository consistent with the Enabling FAIR data Project guidelines prior to publication).* Codes used to make and analyze the VLP catalog are available at crozierjosh1@bitbucket.org/crozierjosh1/vlp-seismicity-catalog-codes.git, and the authors will provide updated versions and/or assistance upon request.

Seismic data from 2008-2011 was obtained from the USGS, subsequent seismic data is publicly available from IRIS. GPS data is publicly available from UNAVCO. Tilt-meter data is available at *Johanson* [2020] *(this citation references a DOI that has been reserved for a planned data release, and will be updated prior to publication).* Lava-lake elevation data was obtained from the USGS, and is published up to 2018 in *Patrick et al.* [2019b]. SO_2 data from 2007-2010 is available at *Elias and Sutton* [2012]. SO_2 emission from 2014-2017 is available at *Elias et al.* [2018]. The VLP seismicity catalog extended from the methods of *Dawson et al.* [2014] was obtained from the USGS.

We thank Phil Dawson for providing an extended version of the Kīlauea VLP catalog published in 2014, seismic data from before 2012, and discussions of VLP seismicity categorization. USGS staff including Matt Patrick, Kyle Anderson, and Ingrid Johanson provided lava-lake elevation, tilt-meter, and GPS data, as well as discussions about Kīlauea. Chao Liang and Eric Dunham provided codes and discussions of modeling magma resonance. LK acknowledges support from NSF EAR-1624557.

References

Aki, K., and P. G. Richards (1993), *Quantitative Seismology*, 2 ed., University Science Books.

Aki, K., M. Fehler, and S. Das (1977), Source mechanism of volcanic tremor: fluid-driven crack models and their application to the 1963 kilauea eruption, *Journal of Volcanology and Geothermal Research*, *2*(3), 259–287, doi:10.1016/0377-0273(77)90003-8.

Alsberg, B. K., A. M. Woodward, and D. B. Kell (1997), An introduction to wavelet transforms for chemometricians: A time- frequency approach, doi:10.1016/S0169-7439(97)00029-4.

Anderson, K. R., and M. P. Poland (2016), Bayesian estimation of magma supply, storage, and eruption rates using a multiphysical volcano model: Kīlauea Volcano, 2000–2012, *Earth and Planetary Science Letters*, *447*, 161–171, doi:10.1016/j.epsl.2016.04.029.

Anderson, K. R., M. P. Poland, J. H. Johnson, and A. Miklius (2015), Episodic Deflation–Inflation Events at Kīlauea Volcano and Implications for the Shallow Magma System, in *Hawaiian Volcanoes*, chap. 11, pp. 229–250, American Geophysical Union (AGU), doi:10.1002/9781118872079.ch11.

Anderson, K. R., I. A. Johanson, M. R. Patrick, M. Gu, P. Segall, M. P. Poland, E. K. Montgomery-Brown, and A. Miklius (2019), Magma reservoir failure and the onset of caldera collapse at Kīlauea Volcano in 2018, *Science*, *366*(6470), eaaz1822, doi:10.1126/science.aaz1822.

Aster, R., D. Zandomeneghi, S. Mah, S. McNamara, D. B. Henderson, H. Knox, and K. Jones (2008), Moment tensor inversion of very long period seismic signals from Strombolian eruptions of Erebus Volcano, *Journal of Volcanology and Geothermal Research*, *177*(3), 635–647, doi:10.1016/j.jvolgeores.2008.08.013.

Baker, S., and F. Amelung (2012), Top-down inflation and deflation at the summit of Klauea Volcano, Hawaii observed with InSAR, *Journal of Geophysical Research B: Solid Earth*, *117*(12), n/a–n/a, doi:10.1029/2011JB009123.

Battaglia, J. (2003), Location of long-period events below Kilauea Volcano using seismic amplitudes and accurate relative relocation, *Journal of Geophysical Research*, *108*(B12), doi:10.1029/2003jb002517.

Bauer, H. F. (1981), Liquid oscillations with a free surface in wedge-shaped tanks, *Acta Mechanica*, *38*(1-2), 31–54, doi:10.1007/BF01351461.

B.Chouet, R. M. (2013), A multi-decadal view of seismic methods for detecting precursors of magma movement and eruption, *Journal of Volcanology and Geothermal Research*, *252*, 108–175, doi:10.1016/j.jvolgeores.2012.11.013.

Bell, J. (2014), *Machine Learning*, John Wiley & Sons, Inc, Indianapolis, IN, USA, doi: 10.1002/9781119183464.

Bergen, K. J., and G. C. Beroza (2019), Earthquake Fingerprints: Extracting Waveform Features for Similarity-Based Earthquake Detection, *Pure and Applied Geophysics*, *176*(3), 1037–1059, doi:10.1007/s00024-018-1995-6.

Berger, J., P. Davis, and G. Ekström (2004), Ambient Earth noise: A survey of the Global Seismographic Network, *Journal of Geophysical Research: Solid Earth*, *109*(11), 1–10, doi:10.1029/2004JB003408.

Brooks, B. A., J. Foster, D. Sandwel, C. J. Wolfe, P. Okubo, M. Poland, and D. Myer (2008), Magmatically triggered slow slip at Kilauea Volcano, Hawaii, doi: 10.1126/science.1159007.

Burgisser, A., B. Scaillet, and Harshvardhan (2008), Chemical patterns of erupting silicic magmas and their influence on the amount of degassing during ascent, *Journal of Geophysical Research: Solid Earth*, *113*(12), B12,204, doi:10.1029/2008JB005680.

Carbone, D., and M. P. Poland (2012), Gravity fluctuations induced by magma convection at Kīlauea volcano, Hawai'i, *Geology*, *40*(9), 803–806, doi:10.1130/G33060.1.

Carbone, D., M. P. Poland, M. R. Patrick, and T. R. Orr (2013), Continuous gravity measurements reveal a low-density lava lake at Kīlauea Volcano, Hawai‘i, *Earth and Planetary Science Letters*, *376*, 178–185, doi:https://doi.org/10.1016/j.epsl.2013.06.024.

Chevrel, M. O., A. J. Harris, M. R. James, L. Calabrò, L. Gurioli, and H. Pinkerton (2018), The viscosity of pahoehoe lava: In situ syn-eruptive measurements from Kilauea, Hawaii, *Earth and Planetary Science Letters*, *493*, 161–171, doi: 10.1016/j.epsl.2018.04.028.

Chouet, B., P. Dawson, Chouet B., and P. Dawson (2011), Shallow conduit system at Kilauea Volcano, Hawaii, revealed by seismic signals associated with degassing bursts, *JGR*, *116*(12), B12,317, doi:10.1029/2011JB008677.

Chouet, B., P. Dawson, Chouet B., and P. Dawson (2013), Very long period conduit oscillations induced by rockfalls at Kilauea Volcano, Hawaii, *JGR Solid Earth*, *118*(10), 5352–5371, doi:10.1002/jgrb.50376.

Chouet, B. A. (1996), Long-period volcano seismicity: Its source and use in eruption forecasting, doi:10.1038/380309a0.

Chouet, B. A., P. B. Dawson, M. R. James, and S. J. Lane (2010), Seismic source mechanism of degassing bursts at Kilauea Volcano, Hawaii: Results from waveform inversion in the 10–50 s band, *JGR*, *115*, doi:10.1029/2009JB006661.

Dawson, P., B. Chouet, Chouet B., and P. Dawson (2014), Characterization of very-long-period seismicity accompanying summit activity at Kīlauea Volcano, Hawai'i: 2007–2013, *Journal of Volcanology and Geothermal Research*, *278-279*, 59–85, doi: 10.1016/j.jvolgeores.2014.04.010.

Dawson, P. B., B. A. Chouet, P. G. Okubo, A. Villaseñor, and H. M. Benz (1999), Three-dimensional velocity structure of the Kilauea Caldera, Hawaii, *GRL*, *26*(18), 2805–2808, doi:10.1029/1999GL005379.

Dawson, P. B., M. C. Benítez, B. A. Chouet, D. Wilson, and P. G. Okubo (2010), Monitoring very-long-period seismicity at Kilauea Volcano, Hawaii, *Geophysical Research Letters*, *37*(18), n/a–n/a, doi:10.1029/2010GL044418.

Edmonds, M., I. R. Sides, D. A. Swanson, C. Werner, R. S. Martin, T. A. Mather, R. A. Herd, R. L. Jones, M. I. Mead, G. Sawyer, T. J. Roberts, A. J. Sutton, and T. Elias (2013), Magma storage, transport and degassing during the 2008–10 summit eruption at Kīlauea Volcano, Hawai'i, *Geochimica et Cosmochimica Acta*, *123*, 284–301, doi: https://doi.org/10.1016/j.gca.2013.05.038.

Elias, T., and A. J. Sutton (2012), Sulfur dioxide emission rates from Kilauea Volcano, Hawai'i, 2007–2010, *U.S. Geological Survey Open-File Report 2012-1107*, p. 25 p.

Elias, T., C. Kern, K. A. Horton, A. J. Sutton, and H. Garbeil (2018), Measuring SO2 Emission Rates at Kīlauea Volcano, Hawaii, Using an Array of Upward-Looking UV Spectrometers, 2014–2017, *Frontiers in Earth Science*, *6*, 214, doi: 10.3389/feart.2018.00214.

Fowler, A. C., and M. Robinson (2018), Counter-current convection in a volcanic conduit, *Journal of Volcanology and Geothermal Research*, *356*, 141–162, doi: 10.1016/j.jvolgeores.2018.03.004.

Giordano, D., J. K. Russell, and D. B. Dingwell (2008), Viscosity of magmatic liquids: A model, *Earth and Planetary Science Letters*, *271*(1-4), 123–134, doi: 10.1016/j.epsl.2008.03.038.

Gonnermann, H. M., and M. Manga (2009), Dynamics of magma ascent in the volcanic conduit, in *Modeling Volcanic Processes: The Physics and Mathematics of Volcanism*, vol. 9780521895, pp. 55–84, Cambridge University Press, doi: 10.1017/CBO9781139021562.004.

Gonnermann, H. M., and M. Manga (2013), *Dynamics of magma ascent in the volcanic conduit*, 55–84 pp., Caimbridge University Pressa, doi: https://doi.org/10.1017/CBO9781139021562.004.

Goodfellow, I., Y. B. Bengio, and A. Courville (2016), *Deep Learning*, MIT Press.

Harris, A. J. (2008), Modeling lava lake heat loss, rheology, and convection, *Geophysical Research Letters*, *35*(7), n/a–n/a, doi:10.1029/2008GL033190.

Hellweg, M. (2000), Physical models for the source of Lascar's harmonic tremor, *Journal of Volcanology and Geothermal Research*, *101*(1-2), 183–198, doi:10.1016/S0377-0273(00)00163-3.

Huber, C., Y. Su, C. T. Nguyen, A. Parmigiani, H. M. Gonnermann, and J. Dufek (2014), A new bubble dynamics model to study bubble growth, deformation, and coalescence, *Journal of Geophysical Research: Solid Earth*, *119*(1), 216–239, doi: 10.1002/2013JB010419.

Iacono-Marziano, G., Y. Morizet, E. Le Trong, and F. Gaillard (2012), New experimental data and semi-empirical parameterization of H 2O-CO 2 solubility in mafic melts, *Geochimica et Cosmochimica Acta*, *97*, 1–23, doi:10.1016/j.gca.2012.08.035.

Ibrahim, R. A. (2005), *Liquid sloshing dynamics*, vol. 9780521838, 1–948 pp., Cambridge University Press, doi:10.1017/CBO9780511536656.

James, M. R., S. J. Lane, and S. B. Corder (2008), Modelling the rapid near-surface expansion of gas slugs in low-viscosity magmas, *Geological Society Special Publication*, *307*(1), 147–167, doi:10.1144/SP307.9.

Jennings, S., D. Hasterok, and J. Payne (2019), A new compositionally based thermal conductivity model for plutonic rocks, *Geophysical Journal International*, *219*(2), 1377–1394, doi:10.1093/gji/ggz376.

Johanson, I. A. (2020), Planned USGS Data Release: doi.org/10.5066/P9LBDSDM, doi: https://doi.org/10.5066/P9LBDSDM.

Johanson, I. A., A. Miklius, and M. P. Poland (2016), Principle component analysis to separate deformation signals from multiple sources during a 2015 intrusive sequence at Kilauea Volcano, *AGUFM*, *2016*, G14A–02.

Jones, J., R. Carniel, A. J. Harris, and S. Malone (2006), Seismic characteristics of variable convection at Erta 'Ale lava lake, Ethiopia, *Journal of Volcanology and Geothermal Research*, *153*(1-2 SPEC. ISS.), 64–79, doi:10.1016/j.jvolgeores.2005.08.004.

Julian, B. R. (1994), Volcanic tremor: nonlinear excitation by fluid flow, *Journal of Geophysical Research*, *99*(B6), doi:10.1029/93jb03129.

Karlstrom, L., and M. Manga (2006), Origins and implications of zigzag rift patterns on lava lakes, *Journal of Volcanology and Geothermal Research*, *154*(3-4), 317–324, doi:10.1016/j.jvolgeores.2006.01.004.

Karlstrom, L., E. M. Dunham, and E. D. L. Karlstrom (2016), Excitation and resonance of acoustic-gravity waves in a column of stratified, bubbly magma, *Journal of Fluid Mechanics*, *797*, 431–470, doi:10.1017/jfm.2016.257.

Knox, H. A., J. A. Chaput, R. C. Aster, and P. R. Kyle (2018), Multiyear Shallow Conduit Changes Observed With Lava Lake Eruption Seismograms at Erebus Volcano, Antarctica, *Journal of Geophysical Research: Solid Earth*, *123*(4), 3178–3196, doi:10.1002/2017JB015045.

Köcher, S. S., T. Heydenreich, and S. J. Glaser (2014), Visualization and analysis of modulated pulses in magnetic resonance by joint time-frequency representations, *Journal of Magnetic Resonance*, *249*, 63–71, doi:10.1016/j.jmr.2014.10.004.

Kohler, A., M. Ohrnberger, and F. Scherbaum (2010), Unsupervised pattern recognition in continuous seismic wavefield records using Self-Organizing Maps, *Geophysical Journal International*, *182*(3), 1619–1630, doi:10.1111/j.1365-246X.2010.04709.x.

Kumazawa, M., Y. Imanishi, Y. Fukao, M. Furumoto, and A. Yamamoto (1990), A theory of spectral analysis based on the characteristic property of a linear dynamic system, *Geophysical Journal International*, *101*(3), 613–630, doi:10.1111/j.1365-246X.1990.tb05574.x.

Lapins, S., D. C. Roman, J. Rougier, S. De Angelis, K. V. Cashman, and J. M. Kendall (2020), An examination of the continuous wavelet transform for volcano-seismic spectral analysis, *Journal of Volcanology and Geothermal Research*, *389*, 106,728, doi:10.1016/j.jvolgeores.2019.106728.

Lesage, P. (2009), Interactive Matlab software for the analysis of seismic volcanic signals, *Computers and Geosciences*, *35*(10), 2137–2144, doi:10.1016/j.cageo.2009.01.010.

Lesage, P., F. Glangeaud, and J. Mars (2002), Applications of autoregressive models and time-frequency analysis to the study of volcanic tremor and long-period events, *Jour-*

nal of Volcanology and Geothermal Research, *114*(3-4), 391–417, doi:10.1016/S0377-0273(01)00298-0.

Liang, C., and E. M. Dunham (2020), Lava lake sloshing modes during the 2018 Kīlauea Volcano eruption probe magma reservoir storativity, *Earth and Planetary Science Letters*, *535*, 116,110, doi:10.1016/j.epsl.2020.116110.

Liang, C., L. Karlstrom, and E. M. Dunham (2019a), Magma oscillations in a conduit-reservoir system , application to very long period (VLP) seismicity at basaltic volcanoes – Part I : Theory, *Journal of Geophysical Research: Solid Earth*.

Liang, C., J. Crozier, L. Karlstrom, and E. M. Dunham (2019b), Magma oscillations in a conduit-reservoir system, application to very long period (VLP) seismicity at basaltic volcanoes–Part II: Data inversion and interpretation at Kīlauea Volcano, *Journal of Geophysical Research: Solid Earth*, p. 2019JB017456, doi:10.1029/2019JB017456.

Lilly, J. M., and S. C. Olhede (2009), Higher-order properties of analytic wavelets, *IEEE Transactions on Signal Processing*, *57*(1), 146–160, doi:10.1109/TSP.2008.2007607.

Lin, G., P. M. Shearer, R. S. Matoza, P. G. Okubo, and F. Amelung (2014), Three-dimensional seismic velocity structure of Mauna Loa and Kilauea volcanoes in Hawaii from local seismic tomography, *Journal of Geophysical Research: Solid Earth*, *119*(5), 4377–4392, doi:10.1002/2013JB010820.

Llewellin, E. W., and M. Manga (2005), Bubble suspension rheology and implications for conduit flow, *Journal of Volcanology and Geothermal Research*, *143*(1-3), 205–217, doi:10.1016/j.jvolgeores.2004.09.018.

Maeda, Y., M. Takeo, T. Ohminato, T. M. Maeda Y., and T. Ohminato (2011), A waveform inversion including tilt: Method and simple tests, *Geophysical Journal International*, *184*(2), 907–918, doi:10.1111/j.1365-246X.2010.04892.x.

Manga, M., and M. Loewenberg (2001), Viscosity of magmas containing highly deformable bubbles, *Journal of Volcanology and Geothermal Research*, *105*(1-2), 19–24, doi:10.1016/S0377-0273(00)00239-0.

Matoza, R. S., D. Fee, and M. A. Garcs (2010), Infrasonic tremor wavefield of the Pu'u 'O'o crater complex and lava tube system, Hawaii, in April 2007, *Journal of Geophysical Research: Solid Earth*, *115*(12), B12,312, doi:10.1029/2009JB007192.

McNutt, S. R., and D. C. Roman (2015), Volcanic Seismicity, in *The Encyclopedia of Volcanoes*, pp. 1011–1034, Elsevier, doi:10.1016/b978-0-12-385938-9.00059-6.

McTigue, D. F. (1987), Elastic stress and deformation near a finite spherical magma body: Resolution of the point source paradox, *Journal of Geophysical Research: Solid Earth*, *92*(B12), 12,931–12,940, doi:10.1029/JB092iB12p12931.

Miklius, A. (2008), Hawaii GPS Network, doi:https://doi.org/10.7283/T5RR1WGN.

Mogi, K. (1958), Relation between the eruptions of various volcanoes and deformations of the ground surfaces around them, *Bulletin of the Earthquake Research Institute*, *36*, 99–134.

Montagna, C. P., and H. M. Gonnermann (2013), Magma flow between summit and Pu‘u ‘O‘o at Kilauea Volcano, Hawai‘i, *Geochemistry, Geophysics, Geosystems*, *14*(7), 2232–2246, doi:10.1002/ggge.20145.

Montgomery-brown, E. K., M. P. Poland, and A. Miklius (2015), Delicate balance of magmatic-tectonic interaction at Kilauea Volcano, Hawai‘i, revealed from slow slip events, in *Geophysical Monograph Series: Hawaiian Volcanoes: From Source to Surface*, vol. 208, pp. 269–288, Blackwell Publishing Ltd, doi:10.1002/9781118872079.ch13.

Mousavi, S. M., W. Zhu, W. Ellsworth, and G. Beroza (2019), Unsupervised Clustering of Seismic Signals Using Deep Convolutional Autoencoders, *IEEE Geoscience and Remote Sensing Letters*, *16*(11), 1693–1697, doi:10.1109/LGRS.2019.2909218.

Nakano, M., H. Kumagai, M. Kumazawa, K. Yamaoka, and B. A. Chouet (1998), The excitation and characteristic frequency of the long-period volcanic event: An approach based on an inhomogeneous autoregressive model of a linear dynamic system, *Journal of Geophysical Research: Solid Earth*, *103*(B5), 10,031–10,046, doi:10.1029/98jb00387.

Neal, C. A., S. R. Brantley, L. Antolik, J. L. Babb, M. Burgess, K. Calles, M. Cappos, J. C. Chang, S. Conway, L. Desmither, P. Dotray, T. Elias, P. Fukunaga, S. Fuke, I. A. Johanson, K. Kamibayashi, J. Kauahikaua, R. L. Lee, S. Pekalib, A. Miklius, W. Million, C. J. Moniz, P. A. Nadeau, P. Okubo, C. Parcheta, M. R. Patrick, B. Shiro, D. A. Swanson, W. Tollett, F. Trusdell, E. F. Younger, M. H. Zoeller, E. K. Montgomery-Brown, K. R. Anderson, M. P. Poland, J. L. Ball, J. Bard, M. Coombs, H. R. Dietterich, C. Kern, W. A. Thelen, P. F. Cervelli, T. Orr, B. F. Houghton, C. Gansecki, R. Hazlett, P. Lundgren, A. K. Diefenbach, A. H. Lerner, G. Waite, P. Kelly, L. Clor, C. Werner, K. Mulliken, G. Fisher, and D. Damby (2019), Volcanology: The 2018 rift eruption and summit collapse of Kilauea Volcano, *Science*, *363*(6425), 367–374, doi:10.1126/science.aav7046.

Orr, T. R., W. A. Thelen, M. R. Patrick, D. A. Swanson, and D. C. Wilson (2013), Explosive eruptions triggered by rockfalls at Kīlauea volcano, Hawai'i, *Geology*, *41*(2), 207–210, doi:10.1130/G33564.1.

Orr, T. R., M. P. Poland, M. R. Patrick, W. A. Thelen, A. J. Sutton, T. Elias, C. R. Thornber, C. Parcheta, and K. M. Wooten (2015), Kilauea's 5–9 march 2011 Kamoamoa fissure eruption and its relation to 30+ years of activity from Pu'u 'O'o, in *Geophysical Monograph Series*, vol. 208, pp. 393–420, Blackwell Publishing Ltd, doi: 10.1002/9781118872079.ch18.

Pal, R. (2003), Rheological behavior of bubble-bearing magmas, *Earth and Planetary Science Letters*, *207*(1-4), 165–179, doi:10.1016/S0012-821X(02)01104-4.

Patrick, M., D. Wilson, D. Fee, T. Orr, and D. Swanson (2011), Shallow degassing events as a trigger for very-long-period seismicity at Kīlauea Volcano, Hawai'i, *Bulletin of Volcanology*, *73*(9), 1179–1186, doi:10.1007/s00445-011-0475-y.

Patrick, M., T. Orr, K. Anderson, and D. Swanson (2019a), Eruptions in sync: Improved constraints on Kīlauea Volcano's hydraulic connection, *Earth and Planetary Science Letters*, *507*, 50–61, doi:https://doi.org/10.1016/j.epsl.2018.11.030.

Patrick, M., D. Swanson, and T. Orr (2019b), A review of controls on lava lake level: insights from Halema'uma'u Crater, Kīlauea Volcano, doi:10.1007/s00445-019-1268-y.

Patrick, M. R., T. Orr, L. Antolik, L. Lee, and K. Kamibayashi (2014), Continuous monitoring of Hawaiian volcanoes with thermal cameras, *Journal of Applied Volcanology*, *3*(1), 1–19, doi:10.1186/2191-5040-3-1.

Patrick, M. R., K. R. Anderson, M. P. Poland, T. R. Orr, and D. A. Swanson (2015), Lava lake level as a gauge of magma reservoir pressure and eruptive hazard, *Geology*, *43*(9), 831–834, doi:10.1130/G36896.1.

Patrick, M. R., T. Orr, A. J. Sutton, E. Lev, W. Thelen, and D. Fee (2016a), Shallowly driven fluctuations in lava lake outgassing (gas pistoning), Kilauea Volcano, *Earth and Planetary Science Letters*, *433*, 326–338, doi:10.1016/j.epsl.2015.10.052.

Patrick, M. R., T. Orr, D. A. Swanson, and E. Lev (2016b), Shallow and deep controls on lava lake surface motion at Kīlauea Volcano, *Journal of Volcanology and Geothermal Research*, *328*, 247–261, doi:10.1016/j.jvolgeores.2016.11.010.

Perol, T., M. Gharbi, and M. Denolle (2018), Convolutional neural network for earthquake detection and location, *Science Advances*, *4*(2), e1700,578, doi:10.1126/sciadv.1700578.

Poland, M., T. R. Orr, J. P. Kauahikaua, S. R. Brantley, J. L. Babb, M. R. Patrick, C. A. Neal, K. R. Anderson, L. Antolik, M. Burgess, T. Elias, S. Fuke, P. Fukunaga, I. A. Johanson, M. Kagimoto, K. Kamibayashi, L. Lee, A. Miklius, W. Million, C. Moniz, P. G. Okubo, A. J. Sutton, T. J. Takahashi, W. A. Thelen, W. Tollett, and F. A. Trusdell (2016), The 2014-2015 Pahoa lava flow crisis at Kilauea Volcano, Hawai'i: Disaster avoided and lessons learned, *GSA Today*, *26*(2), 4–10, doi:10.1130/GSATG262A.1.

Poland, M. P., and D. Carbone (2016), Insights into shallow magmatic processes at Kilauea Volcano, Hawaii, from a multiyear continuous gravity time series, *Journal of Geophysical Research: Solid Earth*, *121*(7), 5477–5492, doi:10.1002/2016JB013057.

Proakis, J. G., and D. G. Monolakis (1990), *Digital Signal Processing: principles, devices and applications*, Peter Peregrinus Ltd, doi:10.1049/pbce042e.

Richardson, J. P., and G. P. Waite (2013), Waveform inversion of shallow repetitive long period events at Villarrica Volcano, Chile, *Journal of Geophysical Research: Solid Earth*, *118*(9), 4922–4936, doi:10.1002/jgrb.50354.

Ripepe, M., D. D. Donne, R. Genco, G. Maggio, M. Pistolesi, E. Marchetti, G. Lacanna, G. Ulivieri, and P. Poggi (2015), Volcano seismicity and ground deformation unveil the gravity-driven magma discharge dynamics of a volcanic eruption, *Nature Communications*, *6*(1), 1–6, doi:10.1038/ncomms7998.

Schaff, D. P. (2008), Semiempirical statistics of correlation-detector performance, *Bulletin of the Seismological Society of America*, *98*(3), 1495–1507, doi:10.1785/0120060263.

Schwartz, S. Y., and J. M. Rokosky (2007), Slow slip events and seismic tremor at circum-pacific subduction zones, doi:10.1029/2006RG000208.

Segall, P. (2010), *Earthquake and volcano deformation*, Princeton University Press, doi:10.5860/choice.48-0287.

Selesnick, I. W., R. G. Baraniuk, and N. G. Kingsbury (2005), The dual-tree complex wavelet transform, doi:10.1109/MSP.2005.1550194.

Sutton, A. J., and T. Elias (2014), One hundred volatile years of volcanic gas studies at the Hawaiian Volcano Observatory: Chapter 7 in Characteristics of Hawaiian volcanoes, in *Professional Paper 1801*, edited by M. P. Poland, T. J. Takahashi, and C. M. Landowski, chap. 7, pp. 295–320, USGS, doi:10.3133/pp18017.

Unglert, K., and A. M. Jellinek (2015), Volcanic tremor and frequency gliding during dike intrusions at Kilauea-A tale of three eruptions, *Journal of Geophysical Research: Solid Earth*, *120*(2), 1142–1158, doi:10.1002/2014JB011596.

USGS (), USGS: Volcano Hazards Program HVO Kilauea.

USGS (1956), USGS Hawaiian Volcano Observatory (HVO), *Hawaiian Volcano Observatory Network*, doi:https://doi.org/10.7914/SN/HV.

Wang, K., H. S. MacArthur, I. Johanson, E. K. Montgomery-Brown, M. P. Poland, E. C. Cannon, M. A. d'Alessio, and R. Bürgmann (2019), Interseismic Quiescence and Triggered Slip of Active Normal Faults of Kīlauea Volcano's South Flank During 2001–2018, *Journal of Geophysical Research: Solid Earth*, *124*(9), 9780–9794, doi: 10.1029/2019JB017419.

Wech, A. G., W. A. Thelen, and A. M. Thomas (2020), Deep long-period earthquakes generated by second boiling beneath Mauna Kea volcano, *Science (New York, N.Y.)*, *368*(6492), 775–779, doi:10.1126/science.aba4798.

Whitty, R. C., E. Ilyinskaya, E. Mason, P. E. Wieser, E. J. Liu, A. Schmidt, T. Roberts, M. A. Pfeffer, B. Brooks, T. A. Mather, M. Edmonds, T. Elias, D. J. Schneider, C. Oppenheimer, A. Dybwad, P. A. Nadeau, and C. Kern (2020), Spatial and Temporal Variations in SO2 and PM2.5 Levels Around Kīlauea Volcano, Hawai'i During 2007–2018, *Frontiers in Earth Science*, *8*, 36, doi:10.3389/feart.2020.00036.

Witham, F., and E. W. Llewellin (2006), Stability of lava lakes, *Journal of Volcanology and Geothermal Research*, *158*(3-4), 321–332, doi:10.1016/j.jvolgeores.2006.07.004.

Wright, T. L., and F. W. Klein (2014), Two hundred years of magma transport and storage at Kilauea Volcano, Hawai'i, 1790–2008, *U.S. Geological Survey Professional Paper 1806*, p. 240 p., doi:doi:10.3133/pp1806.

Yoon, C. E., O. O'Reilly, K. J. Bergen, and G. C. Beroza (2015), Earthquake detection through computationally efficient similarity search, *Science Advances*, *1*(11), e1501,057, doi:10.1126/sciadv.1501057.

Zadler, B. J., J. H. Le Rousseau, J. A. Scales, and M. L. Smith (2004), Resonant ultrasound spectroscopy: Theory and application, *Geophysical Journal International*, *156*(1), 154–169, doi:10.1111/j.1365-246X.2004.02093.x.

Supporting Information for "Very-long-period seismicity over the 2008-2018 eruption of Kīlauea Volcano"

Josh Crozier[1], Leif Karlstrom[1]

[1]Department of Earth Sciences, University of Oregon, Eugene, Oregon, USA.

Contents

Figures S.1 to S.24, arranged in sections 1: Synthetic waveform test figures, 2: Catalog figures, and 3: Example event figures

Additional Supporting Information (Files uploaded separately)

1. *Kilauea_2008-2018_resonant_signal_catalog_presented.csv*
   A version of our event catalog thresholded to include 3209 events, as presented in the text. The first row contains descriptions of each variable, and the second row contains the names of each variable.
2. *Kilauea_2008-2018_resonant_signal_catalog_full.csv*
   A version of our event catalog thresholded to include 33084 events. The thresholds used in this version are: STA/LTA > 2, standard deviations above the LTA > 1, Q > 4, and mean phase deviation < 0.25 radians. The first row contains descriptions of each variable, and the second row contains the names of each variable.

1 Synthetic waveform test figures

Corresponding author: Josh Crozier, `jcrozier@uoregon.edu`

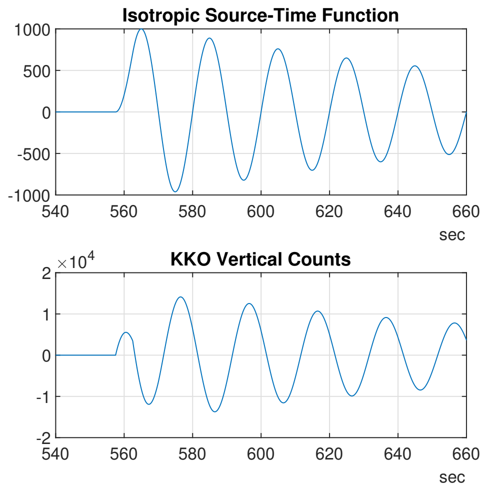

Figure S.1. Example synthetic source-time function and corresponding synthetic seismogram (which has been convolved with the elastic Green's functions and instrument response), zoomed in around the signal onset to show the tapers used (see appendix). This source-time function is for an impulsive onset oscillation with T = 20 s, Q = 20, and no added noise.

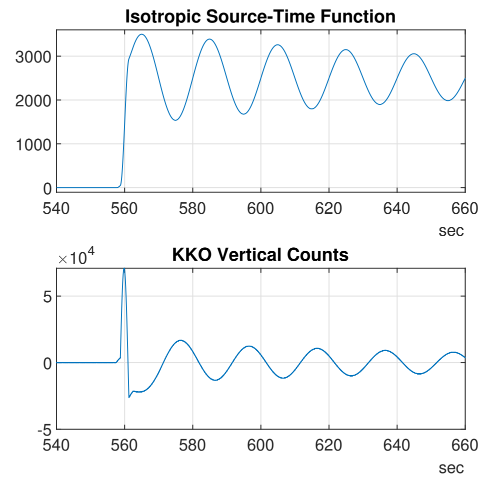

Figure S.2. Example synthetic source-time function and corresponding synthetic seismogram (which has been convolved with the elastic Green's functions and instrument response), zoomed in around the signal onset to show the tapers used (see appendix). This source-time function is for an impulsive onset oscillation with T = 20 s, Q = 20, an added step displacement, and no added noise.

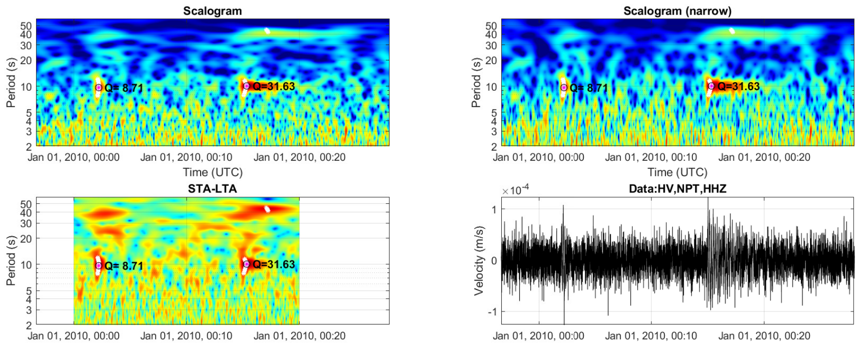

Figure S.3. Example scalograms and detected resonant signals from a synthetic seismogram consisting of four resonant signals with [start time, T, Q] = [00:05, 40, 6], [00:05, 10, 6], [00:15, 40, 40], [00:15, 40, 40], plus white noise from a standard normal distribution scaled by 5.0% of the signal amplitude. At this noise level only two of the signals are found at the detection thresholds used, and the quality factor estimates are less accurate (off by ~25%).

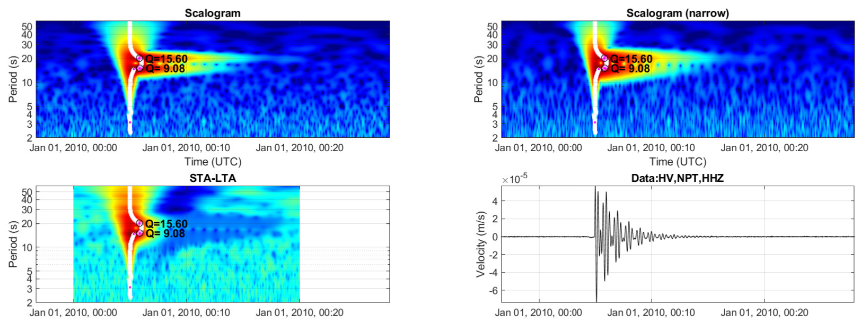

Figure S.4. Example scalograms and detected resonant signals from a synthetic seismogram consisting of two resonant signals with [start time, T, Q] = [00:05, 20, 20], [00:05, 15, 20], plus white noise from a standard normal distribution scaled by 0.1% of the signal amplitude. In this case the spectral proximity of the two signals means that wavelets at the period of one signal are influenced by the other signal, which causes both quality factors to be under-estimated (by 22-54%).

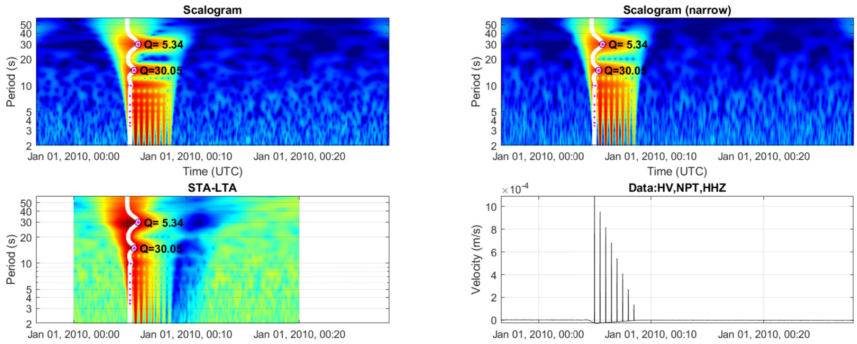

Figure S.5. Example scalograms and detected resonant signals from a synthetic seismogram consisting of eight step displacements (velocity spikes) spaced 30 s apart, plus white noise from a standard normal distribution scaled by 1.0% of the signal amplitude. The closely spaced spikes create a Dirac comb effect, where the spectrum would indicate apparent resonances at 15 s, 7.5 s, 3.25 s, and etc. The temporal resolution of our narrow (β=20) wavelet, which is used for calculating Q, is high enough that apparent resonances with T less than 15 s are not picked.

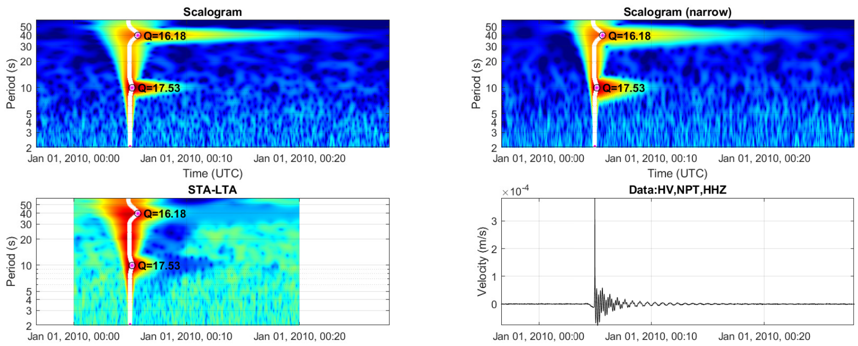

Figure S.6. Example scalograms and detected resonant signals from a synthetic seismogram consisting of a large step displacement (velocity spike) at time 00:05 plus two resonant signals with [start time, T, Q] = [00:05, 40, 20] and [00:05, 10, 20] plus white noise from a standard normal distribution scaled by 0.1% of the signal amplitude. The presence of the step function decreases the estimated quality factors by 12-19% due to the increased energy at the start of the signals, but otherwise does not appreciably impact the results.

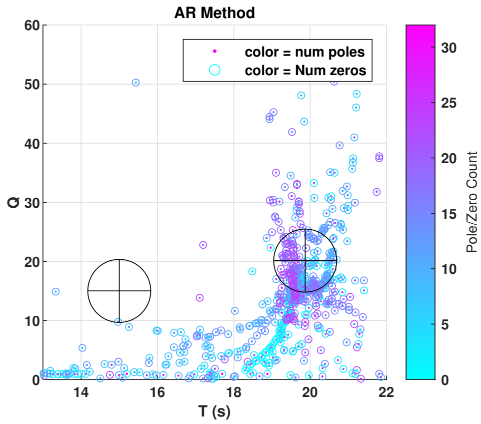

Figure S.7. Example 'Sompi' AR method for estimating T and Q applied to a synthetic seismogram. Code used from Lesage 2009. In this case the method was applied to a data window from 10-200 s following the onset of a 20 s oscillation with Q = 20 and a smaller (by a factor of 4) 15 s oscillation with Q = 15 (indicated by black crosses/circles). Results from filters with 4-32 poles and 0-32 zeros are shown to test a wide parameter space; for practical use narrower ranges would likely be used. A cluster near the actual T and Q of the 20 s oscillation does occur, though mean T and Q values within this cluster are offset from the correct value and exhibit significant scatter. No cluster occurs near the smaller 15 s oscillation, so it would be missed entirely by this AR method.

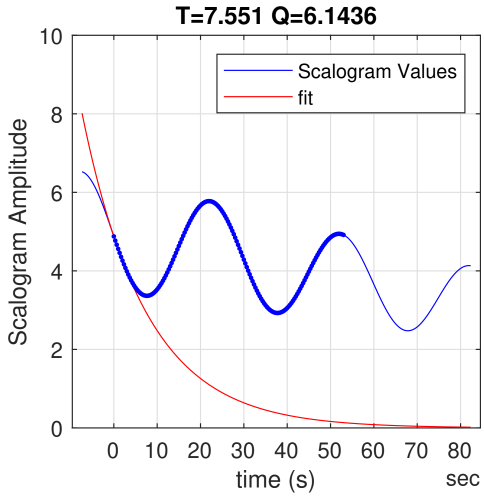

Figure S.8. Example estimation of Q by scalogram exponential fit. Applied to synthetic seismograms consisting of a series of tapered step displacements (velocity spikes) spaced 30 s apart, plus white noise from a standard normal distribution scaled by 0.1% of the signal amplitude. The closely spaced spikes create a Dirac comb effect, where the frequency spectrum would indicate apparent resonances at 15 s, 7.5 s, 3.25 s, and etc. The time resolution of the β=20 wavelet we use for calculating Q is sufficient to distinguish gaps in this apparent 7.5 s resonance, so our fit avoids overestimating Q as a standard least-squares exponential regression would.

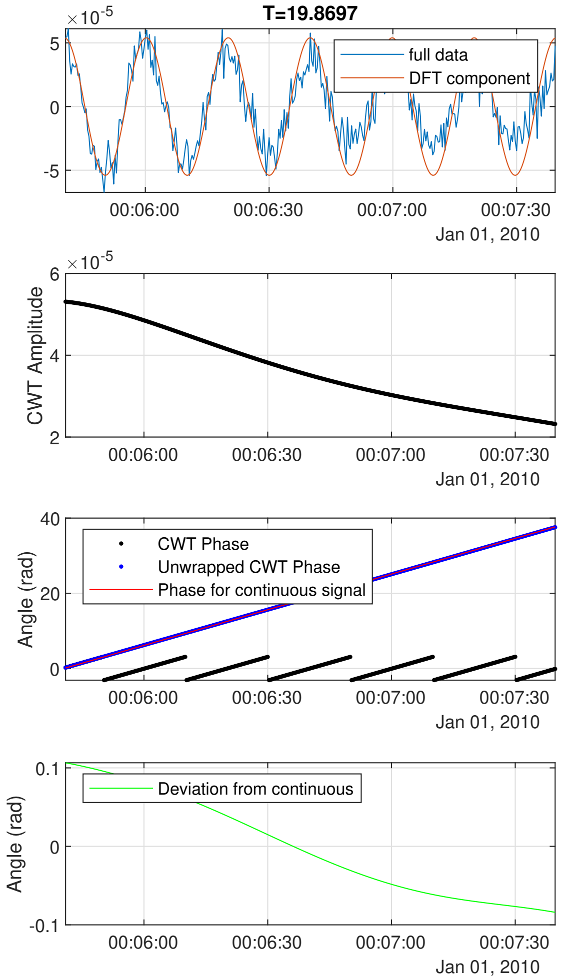

Figure S.9. Example phase continuity from a synthetic seismogram consisting of a resonant signal with T=20 s and Q=20, plus white noise from a standard normal distribution scaled by 0.1% of the signal amplitude. In this case the phase deviation is small (mean of around 0.05 radians), correctly indicating that this is likely a continuous oscillation.

2 Catalog figures

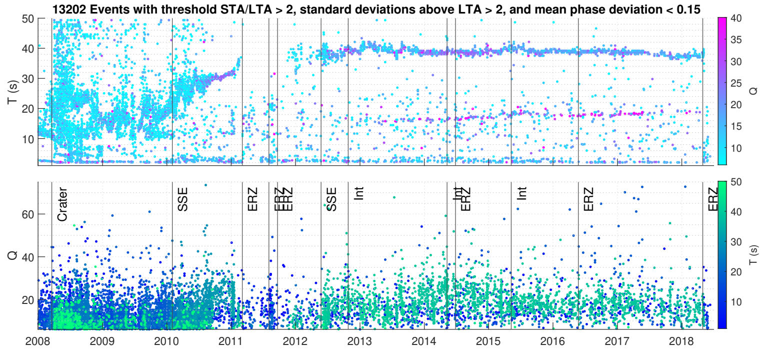

Figure S.10. Resonant signal catalog from 2008-2018 with less strict event detection thresholds than presented in the main text. 'Crater' indicates where the Halema'uma'u crater first formed, 'SSE' indicates slow slip events, 'Int' indicates documented summit intrusions, and 'ERZ' indicates eruptions along the East-Rift-Zone.

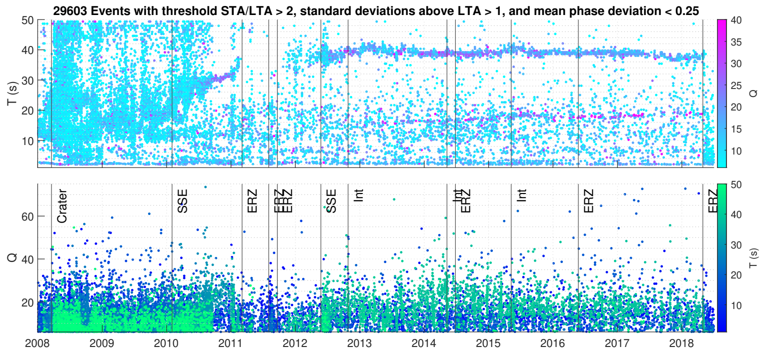

Figure S.11. Resonant signal catalog from 2008-2018 with less strict event detection thresholds than presented in the main text. 'Crater' indicates where the Halema'uma'u crater first formed, 'SSE' indicates slow slip events, 'Int' indicates documented summit intrusions, and 'ERZ' indicates eruptions along the East-Rift-Zone.

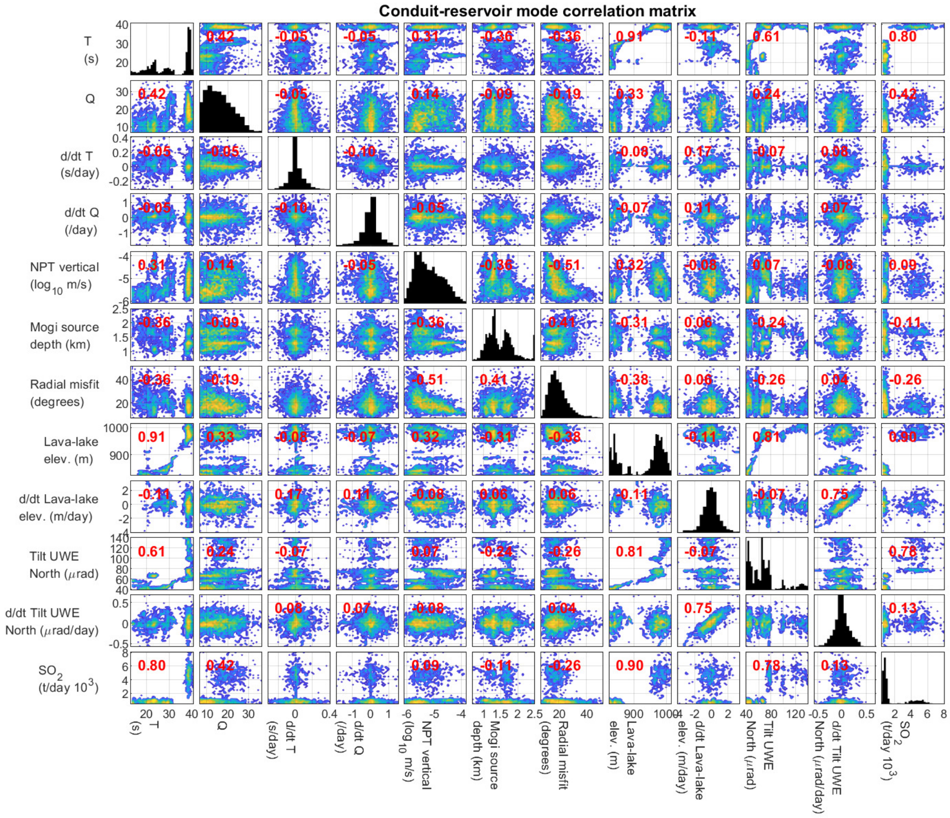

Figure S.12. Conduit-reservoir mode correlation matrices from 2008-2018. Off-diagonal plots are colored by the logarithm of the number of points in a given parameter bin, and histograms on diagonal plots show the distribution of each parameter. Red numbers are Pearson's correlation coefficients, only shown for correlations with P-values less than 0.05. All time derivatives were calculated with a 7-day cutoff-period differentiator filter (see Methods section).

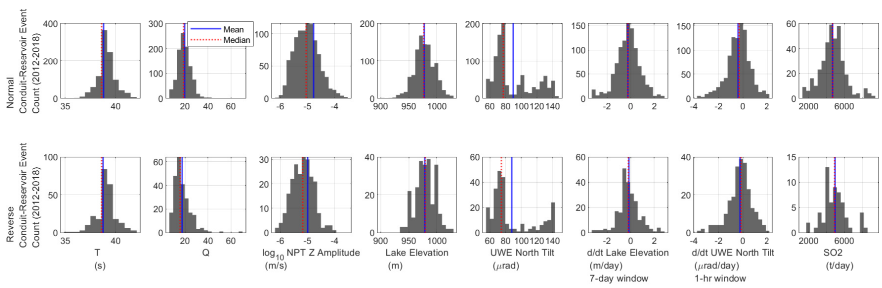

Figure S.13. Histograms of Normal and Reverse conduit-reservoir mode event parameters from 2012-2018.

3 Example event figures

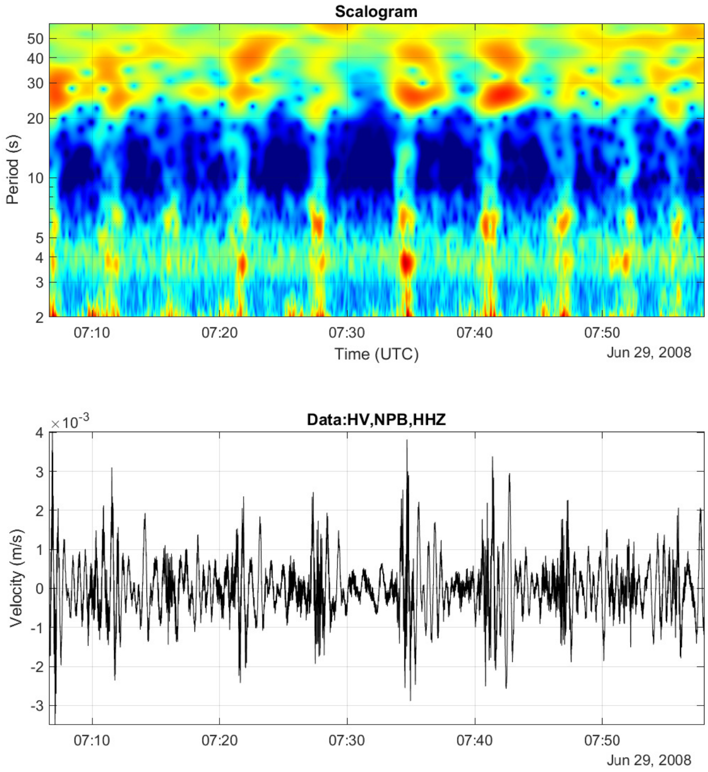

Figure S.14. VLP events with regular recurrence interval from June 2008, a few months after the Overlook Crater began forming. These events occurred roughly every 5 minutes and contained broadband energy with spectral peaks at around 3.5 s, 6 s, 25 s, and possibly 40 s. These events exhibited less clear onsets and exponential decays than typical rockfall-triggered events.

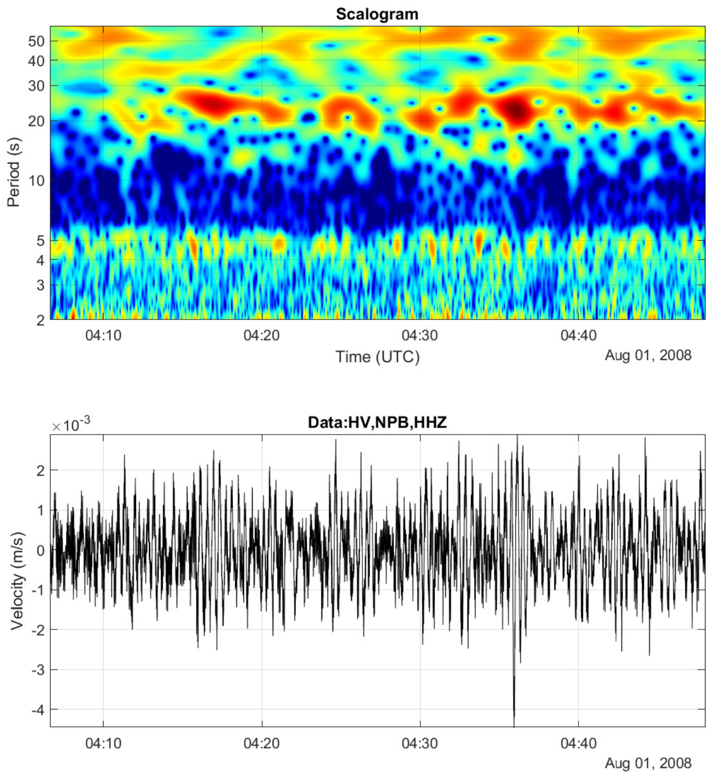

Figure S.15. VLP tremor from August 2008, in the first focused cluster of VLP signals. There was elevated energy at periods from 15-30 s and 4-5 s, though the dominant periods were not clearly focused and were variable over time. The signal cannot readily be separated into distinct events, and exhibited no clear high frequency triggers.

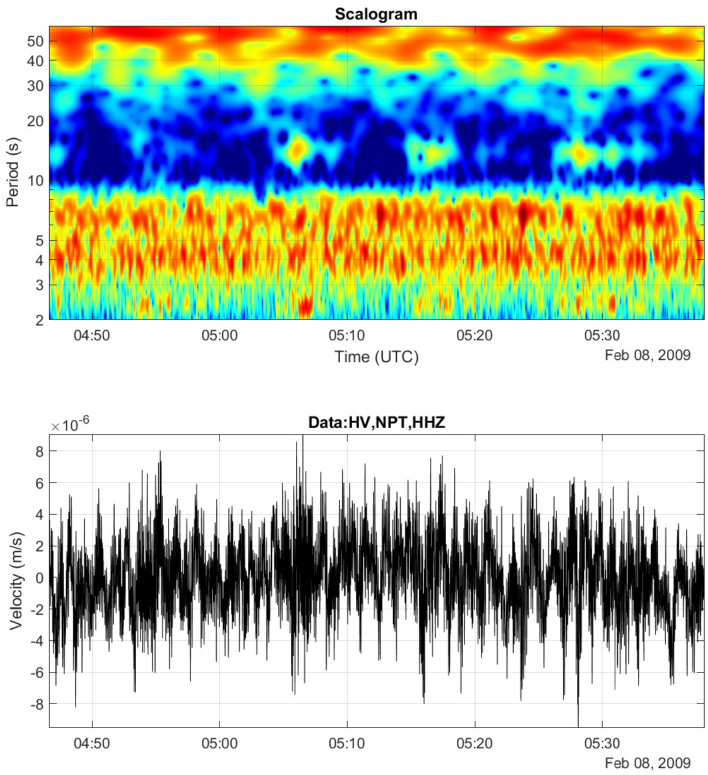

Figure S.16. VLP events from February 2009, around the time where dominant VLP period is at a minimum. These appear to be distinct VLP events, thought onsets of some were gradual and first motions were not well defined. Elevated energy at periods < 2 s occurred alongside these signals, but did not appear to represent the more broadband impulsive trigger mechanisms that occur at the onset of typical rockfall events.

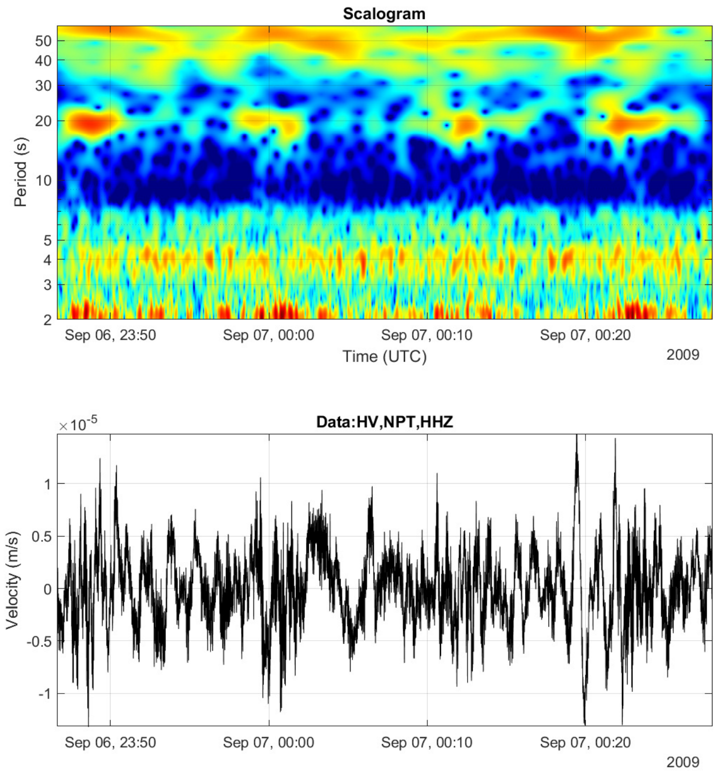

Figure S.17. VLP tremor from September 2009, in a signal cluster that seems to represent a local maxima in VLP period (around 20 s).

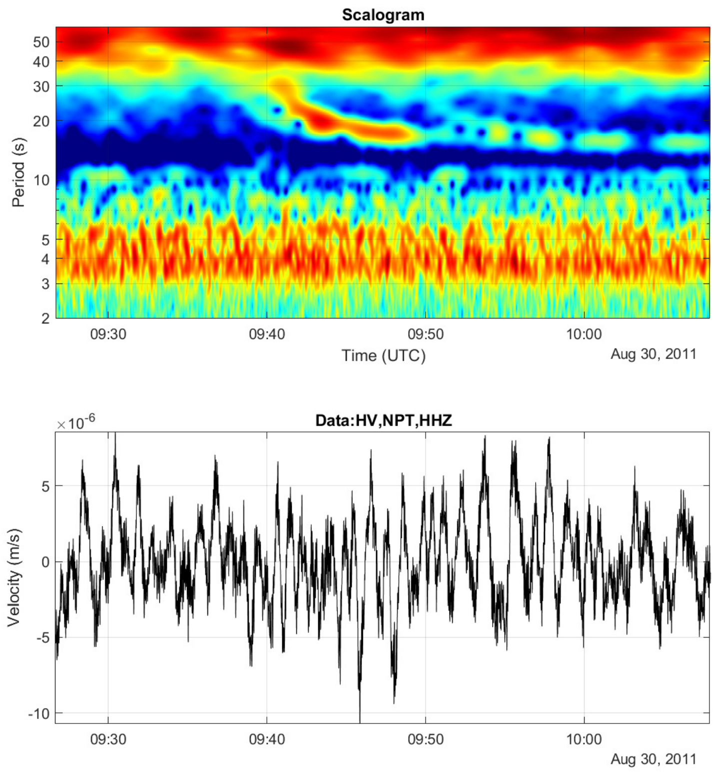

Figure S.18. Gliding-frequency VLP signal from August 2011, part of a small cluster of VLP seismicity following the August 2011 Pu‘u ‘Ō‘ō eruption. This event had no apparent high frequency trigger. VLP energy remained elevated for 10s of minutes after the event, though this energy did not appear to represent continuous decay of the initial resonance but rather continued intermittent forcing, perhaps partly by what may be a second smaller gliding-frequency signal around 10 minutes after the first. There was also background VLP tremor present with a period of around 11 s that does not appear to have been effected by the gliding-frequency event.

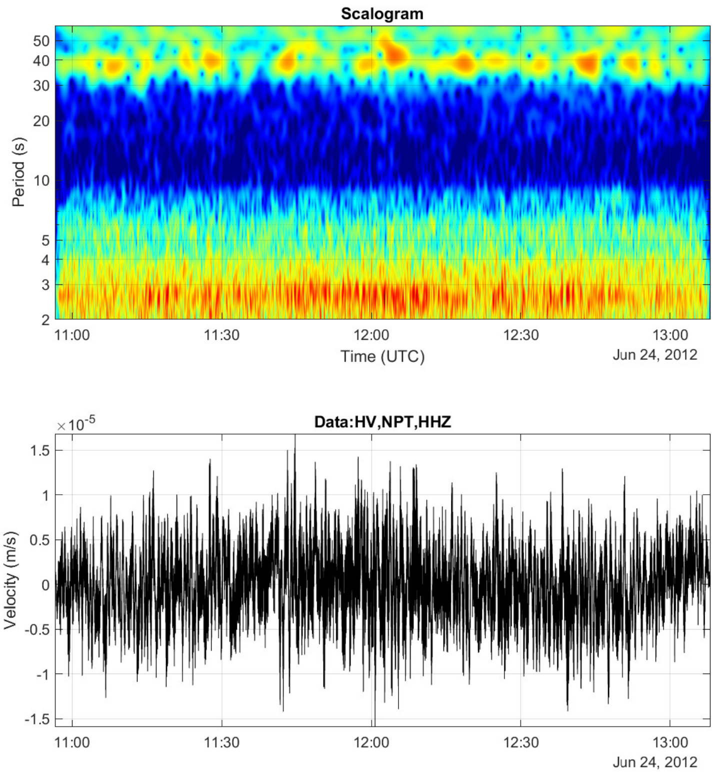

Figure S.19. VLP tremor from June 2012, shortly after the May SSE and around when higher Q VLP events start occurring again after a year with minimal VLP seismicity.

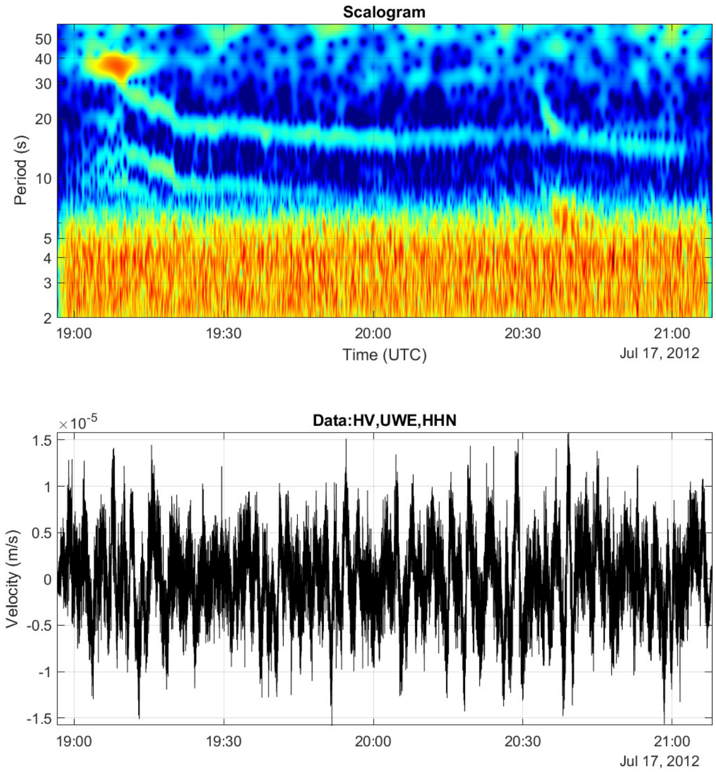

Figure S.20. Gliding-frequency VLP signals from July 2012. There was a set of three resonant modes starting around 19:10, and a single resonant mode that started about 90 minutes later. No high frequency triggers were apparent. The first 3 modes all exhibited a similar glide to lower periods over about 10 minutes, then maintained more stable periods. The later mode had a more rapid initial glide to lower periods (over about 5 minutes) but then continued more slowly gliding for another 20 minutes.

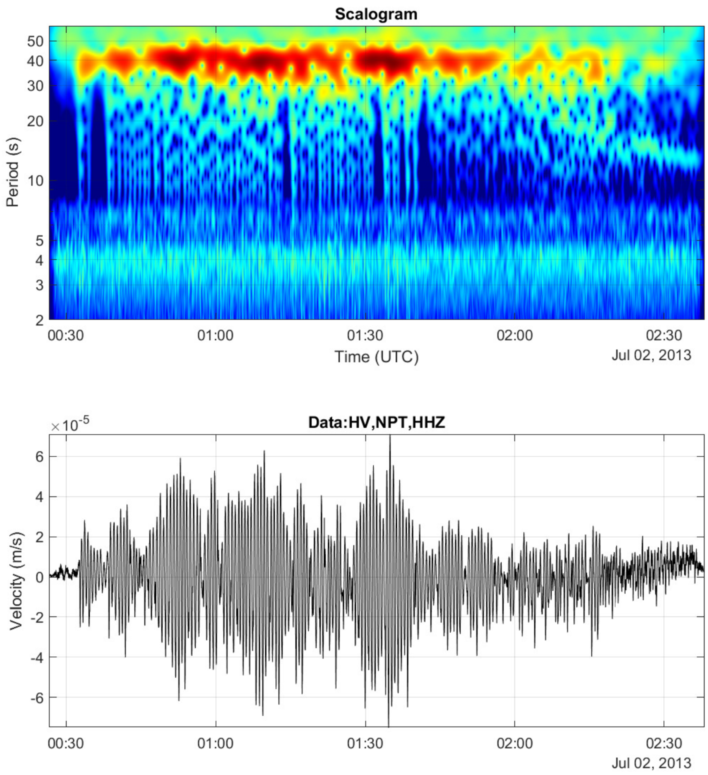

Figure S.21. VLP event/tremor from July 2013. This signal consisted of sustained 40 s oscillations at varying amplitudes and irregular bursts of higher frequency energy. These bursts were much weaker relative to the main VLP oscillation than typical rockfall trigger signals. The main VLP signal had an impulsive onset with deflationary first motions.

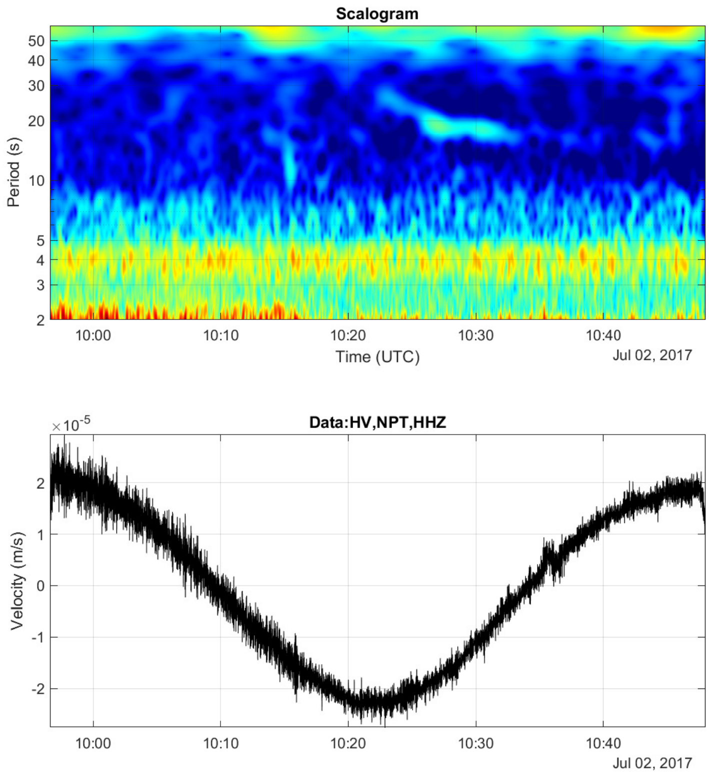

Figure S.22. Isolated lake sloshing mode with possible gliding-frequency onset from July 2017.

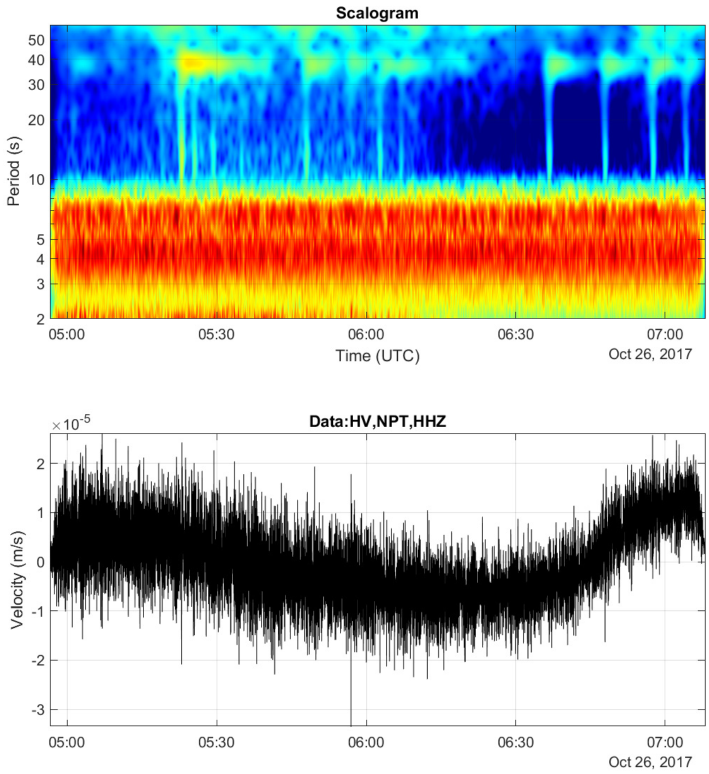

Figure S.23. Closely spaced Normal conduit-reservoir events from October 2017. These may have represented a series of small rockfalls.

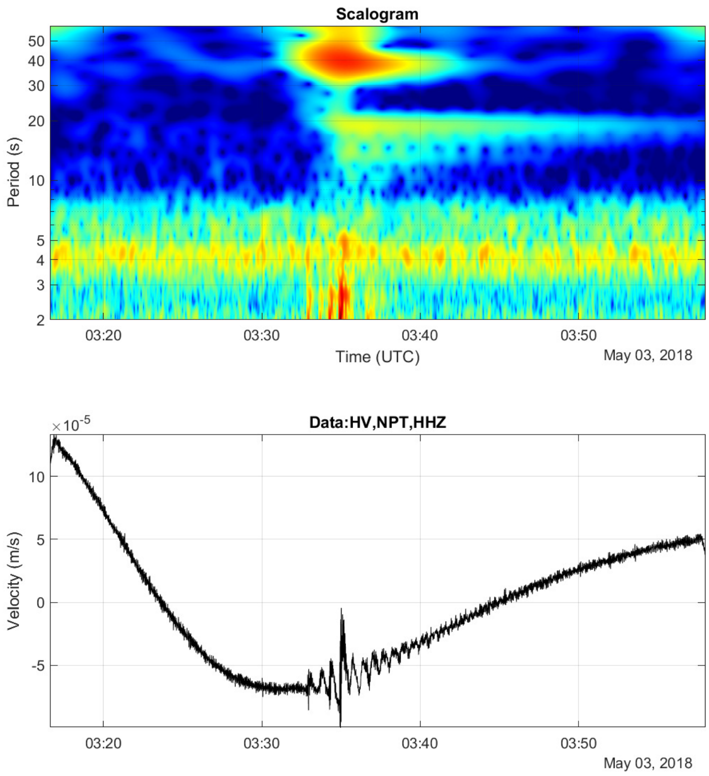

Figure S.24. VLP event with two clear lava-lake-sloshing modes from May 2018, a day after the lava-lake began draining. The dominant 40 s mode for this event started with impulsive inflationary motions, though with only a very faint high frequency trigger, but then grew for several minutes until a second impulse occurred and exponential decay began. The lava-lake-sloshing modes appeared alongside this second impulse.